

Benchmark tests of MITC triangular shell elements

Hyungmin Jun^{*1}, Paul Mukai² and San Kim³

¹Department of Biological Engineering, Massachusetts Institute of Technology, Cambridge, MA 02139, USA

²PVM Associates, Andover, MA 01810, USA

³Department of Mechanical Engineering, Korea Advanced Institute of Science and Technology, Daejeon 34141, Republic of Korea

(Received June 18, 2018, Revised August 9, 2018, Accepted August 14, 2018)

Abstract. In this paper, we compare and assess the performance of the standard 3- and 6-node MITC shell elements (Lee and Bathe 2004) with the recently developed MITC triangular elements (Lee *et al.* 2014, Jeon *et al.* 2014, Jun *et al.* 2018) which were based on the partitions of unity approximation, bubble node, or both. The convergence behavior of the shell elements are measured in well-known benchmark tests; four plane stress tests (mesh distortion test, cantilever beam, Cook's skew beam, and MacNeal beam), two plate tests (Morley's skew plate and circular plate), and six shell tests (curved beam, twisted beam, pinched cylinder, hemispherical shells with or without hole, and Scordelis-Lo roof). To precisely compare and evaluate the solution accuracy of the shell elements, different triangular mesh patterns and distorted element mesh are adopted in the benchmark problems. All shell finite elements considered pass the basic tests; namely, the isotropy, the patch, and the zero energy mode tests.

Keywords: benchmark test; shell structure; triangular shell element; MITC method; partition of unity; bubble-node

1. Introduction

The finite element method has been used as a powerful numerical tool to analyze shell structures. In the last two decades, a great deal of effort has been expended on improving the solution accuracy for shell finite elements (Choi *et al.* 1999, Yoo and Choi 2000, Han *et al.* 2011). Compared with the quadrilateral element (Choi and Park 1994), the triangular element is particularly attractive due to its geometric simplicity. It also allows for local mesh refinement and automatic mesh generation, both of which facilitate the effective discretization of arbitrary geometries with large curvature. In addition, for the 3-node triangular element, the membrane locking associated with the curved shell can be obviated due to the flat geometric characteristic. However, the optimal solution accuracy obtained by the triangular finite elements was generally not achieved mainly due to two factors; the transverse shear locking and the overly stiff behavior related to the in-plane shear locking (Bathe 2016, Hughes 2012).

The locking phenomenon caused by parasitic internal energy, leading to artificial stiffness, has been thoroughly studied. Especially, the transverse shear-locking occurs usually in displacement-based plate and shell finite elements when the thickness of the element becomes relatively small. Historically, there have been numerous attempts to alleviate the locking of plate and shell finite elements. A major advancement was realized by the MITC (Mixed Interpolation of Tensorial Components) technique

for quadrilateral and triangular plate and shell elements (Lee and Bathe 2004, Lee *et al.* 2014, Jeon *et al.* 2014, Jun *et al.* 2018, Bathe and Dvorkin 1986, Bathe *et al.* 2003, da Veiga *et al.* 2007, Lee *et al.* 2008, Kim and Bathe 2009, Lee *et al.* 2012, Jeon *et al.* 2015, Lee *et al.* 2015, Ko *et al.* 2016, 2017a). Based on the MITC approach, firstly, the MITC3 and MITC6 shell elements (Lee and Bathe 2004) for 3-node and 6-node triangular elements, respectively, were suggested, which are spatially isotropic without a spurious zero energy mode or artificial factor, and pass plate bending and membrane patch tests. However, despite the advantage of this simple formulation and its computational efficiency, the convergence behavior of the MITC3 shell element is significantly diminished in the analysis of bending-dominant problems due to and incomplete transverse locking treatment and its overly stiff membrane behavior.

To remedy this difficulty, great research efforts have been undertaken (Choi *et al.* 1999, da Veiga *et al.* 2007, Kim and Bathe 2009, Lee *et al.* 2012, 2014, Jeon *et al.* 2015). A successful strategy was achieved by introducing a cubic bubble function for the rotations of the MITC3 shell element, which was called MITC3+ (Lee *et al.* 2014, Jeon *et al.* 2015, Lee *et al.* 2015). A newly developed assumed transverse shear strain field for the higher-order interpolation was also suggested to alleviate shear locking. The cubic bubble function provides a higher-order interpolation inside the element to enrich the element behavior while maintaining the linear interpolation along the element edges. It shows excellent performance and convergence behavior in both the linear and the non-linear general shell analyses (Lee *et al.* 2014, Jeon *et al.* 2015, Lee *et al.* 2015, Ko *et al.* 2017b).

Another strategy to yield much more accurate solutions, Jeon *et al.* (2014) developed the enriched MITC3 shell

*Corresponding author, Ph.D.
E-mail: hmjeon@mit.edu

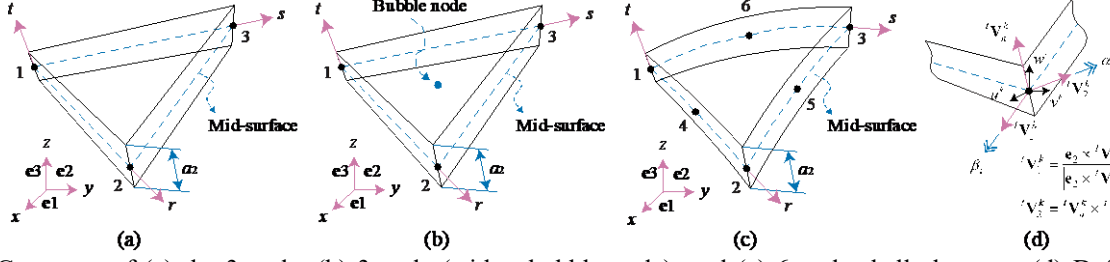


Fig. 1 Geometry of (a) the 3-node, (b) 3-node (with a bubble node), and (c) 6-node shell elements. (d) Definition of rotational degrees of freedom, α_k and β_k

element (hereafter denoted MITC3E) by integrating the PU (partition of unity) approximation with the standard 3-node shell element, MITC3. Within the framework of the PU approximation, construction of high-order interpolations can be achieved in a straightforward manner by directly adopting high-order polynomials as local approximations without utilizing additional nodes along the element sides and inside element. It was reported that the MITC3E shell element performed significantly better than the quadrilateral (4-node) and higher-order triangular (6-node) shell elements in some problems even when using distorted meshes (Jeon *et al.* 2014). A distinguishing feature is that the local use of the partition of unity approximation results in excellent overall accuracy with a significantly reduced number of degrees of freedom (Jeon *et al.* 2014).

Recently, Jun *et al.* (2018) proposed the new 3-node triangular shell finite element (hereafter denoted MITC3E+) based on the MITC3+ shell element by introducing the partition of unity approximation using piecewise polynomials in its membrane displacements. Since the MITC3+ shell element shows excellent performance in the analysis of bending-dominated problems, enriching its membrane behaviors should make the element more generally applicable. As a result, significantly improved membrane performance was achieved by additional four DOFs (degrees of freedom) at each of three corner nodes. Superior performance was observed in both linear and geometric nonlinear analyses (Jun *et al.* 2018).

The aim of this study is to compare the solution accuracy and computational efficiency of the MITC triangular shell elements, through several widely used benchmark problems. The solutions of the recently proposed MITC triangular shell elements based on the partition of unity approximation, the bubble node, or both, are compared to each other and with those of the standard 3-node and 6-node shell elements. The popular benchmark problems including four plane-stress, two plate, and six shell tests are selected from the references (Ko *et al.* 2017b, MacNeal and Harder 1985). Since the solution of the triangular finite elements are highly sensitive to the triangulated pattern and distortion of the element mesh, we not only use various element mesh patterns (constant and mixed directional element meshes) but also properly selected distorted meshes in benchmark problems.

2. The formulation of the MITC triangular shell elements

In this section, we briefly review the formulations of the MITC triangular shell elements, named as MITC3, MITC6, MITC3+, MITC3E, and MITC3E+ shell elements listed in Table 1. All shell elements considered here pass the basic tests; the isotropy, patch, and zero energy mode tests.

2.1 Displacement interpolations

The geometries of continuum mechanics based on triangular shell elements are shown in Fig. 1(a)-(c). The displacement interpolations for the shell elements are obtained from (Lee and Bathe 2004, Lee *et al.* 2014, Jeon *et al.* 2014, Jun *et al.* 2018)

$$\mathbf{u}(r, s, t) = \sum_{i=1}^m h_i^m(r, s) \tilde{\mathbf{u}}_i + \frac{t}{2} \sum_{i=1}^n a_i h_i^n(r, s) \left(-\mathbf{V}_2^i \tilde{\alpha}_i + \mathbf{V}_1^i \tilde{\beta}_i \right), \quad (1)$$

where m and n represent the number of element nodes that correspond to the translations and rotations, respectively, h_i^m and h_i^n are the two-dimensional shape functions of the isoparametric procedure corresponding to node i . a_i denotes the shell thickness at node i , and \mathbf{V}_1^i and \mathbf{V}_2^i are the unit vectors orthogonal to the director vector \mathbf{V}_n^i and to each other. $\tilde{\mathbf{u}}_i$ is the nodal displacement vector, and $\tilde{\alpha}_i$ and $\tilde{\beta}_i$ are the rotations of the director at node i . Each shell finite element has the following parameters m and n , nodal displacement vector and rotations:

- MITC3: $m=3, n=3$, $\tilde{\alpha}_i = \alpha_i$, $\tilde{\beta}_i = \beta_i$, $\tilde{\mathbf{u}}_i = \mathbf{u}_i$,
- MITC6: $m=6, n=6$, $\tilde{\alpha}_i = \alpha_i$, $\tilde{\beta}_i = \beta_i$, $\tilde{\mathbf{u}}_i = \mathbf{u}_i$,
- MITC3+: $m=3, n=4$, $\tilde{\alpha}_i = \alpha_i$, $\tilde{\beta}_i = \beta_i$, $\tilde{\mathbf{u}}_i = \mathbf{u}_i$,
- MITC3E: $m=3, n=3$, $\tilde{\alpha}_i = \alpha_i + \zeta_i \alpha_i^\xi + \eta_i \alpha_i^\eta$,
 $\tilde{\beta}_i = \beta_i + \zeta_i \beta_i^\xi + \eta_i \beta_i^\eta$, $\tilde{\mathbf{u}}_i = \mathbf{u}_i + \zeta_i \mathbf{u}_i^\xi + \eta_i \mathbf{u}_i^\eta$,
- MITC3E+: $m=3, n=3$, $\tilde{\alpha}_i = \alpha_i$, $\tilde{\beta}_i = \beta_i$,
 $\tilde{\mathbf{u}}_i = \mathbf{u}_i + (\zeta_i \mathbf{u}_i^\xi + \eta_i \mathbf{u}_i^\eta) \mathbf{V}_1^i + (\zeta_i \mathbf{v}_i^\xi + \eta_i \mathbf{v}_i^\eta) \mathbf{V}_2^i$.

In the above, $\mathbf{u}_i = [u_i \ v_i \ w_i]^T$ is the standard nodal displacement vector in the global Cartesian coordinate system, α_i and β_i are the standard rotations of the director vector \mathbf{V}_n^i about \mathbf{V}_1^i and \mathbf{V}_2^i , respectively, at

Table 1 A list of MITC triangular shell finite elements used for comparison

Element type	Descriptions	# of DOFs / node	# of DOFs / bubble node	# of tying points for assumed strain
MITC3	Standard 3-node MITC shell element (Lee and Bathe 2004)	5	-	3
MITC6	Standard 6-node MITC shell element (Lee and Bathe 2004)	5	-	16
MITC3+	3-node MITC shell element with a bubble node (Lee <i>et al.</i> 2014)	5	2	6
MITC3E	PU based 3-node MITC shell element (Jeon <i>et al.</i> 2014)	15	-	9
MITC3E+	MITC3+ shell element enriched in membrane displacement by the PU approximation (Jun <i>et al.</i> 2018)	9	2	6

node i . In the MITC3E and MITC3E+ shell elements, $\mathbf{u}_i^\xi = [u_i^\xi \ v_i^\xi \ w_i^\xi]^T$ and $\mathbf{u}_i^\eta = [u_i^\eta \ v_i^\eta \ w_i^\eta]^T$ are the enriched nodal displacement vectors and α_i^ξ , α_i^η , β_i^ξ , and β_i^η are the enriched rotations. The ξ_i and η_i are defined by

$$\xi_i = (\mathbf{x} - \mathbf{x}_i) \cdot \mathbf{V}_1^i / \tilde{h}_i, \quad \eta_i = (\mathbf{x} - \mathbf{x}_i) \cdot \mathbf{V}_2^i / \tilde{h}_i, \quad (2)$$

in which \tilde{h}_i is a characteristic element length scale of the elements used in the mesh (Jeon *et al.* 2014, Jun *et al.* 2018, Duarte *et al.* 2000, Kim and Bathe 2013). The shape functions, h_i^m and h_i^n are used as follows

$$h_1^3 = 1 - r - s, \quad h_2^3 = r, \quad h_3^3 = s, \quad (3a)$$

$$h_1^4 = h_1^3 - \frac{1}{3}h_4^4, \quad h_2^4 = h_2^3 - \frac{1}{3}h_4^4, \quad (3b)$$

$$h_3^4 = h_3^3 - \frac{1}{3}h_4^4, \quad h_4^4 = 27rs(1 - r - s)$$

$$h_1^6 = 1 - r - s - \frac{1}{2}h_4^6 - \frac{1}{2}h_6^6,$$

$$h_2^6 = r - \frac{1}{2}h_4^6 - \frac{1}{2}h_5^6, \quad h_3^6 = s - \frac{1}{2}h_5^6 - \frac{1}{2}h_6^6 \quad (3c)$$

$$h_4^6 = 4r(1 - r - s), \quad h_5^6 = 4rs, \quad \text{and} \quad h_6^6 = 4s(1 - r - s).$$

Note that the displacement interpolations for the MITC3E and MITC3E+ shell elements can be divided into two parts: the linear term $\bar{\mathbf{u}}$ and the additional quadratic term $\hat{\mathbf{u}}$, as

$$\mathbf{u}(r, s, t) = \bar{\mathbf{u}}(r, s, t) + \hat{\mathbf{u}}(r, s, t). \quad (4)$$

The linear term $\bar{\mathbf{u}}$ for the MITC3E and MITC3E+ shell elements can be replaced with the displacement interpolations of the MITC3 and MITC3+ shell elements, respectively, resulting in the quadratic terms $\hat{\mathbf{u}}$: (Eq. (5a)) for the MITC3E element and Eq. (5b) for the MITC3E+ element)

$$\begin{aligned} \hat{\mathbf{u}} = & \sum_{i=1}^3 h_i^3(r, s) \left[\xi_i \mathbf{u}_i^\xi \quad \eta_i \mathbf{u}_i^\eta \right] \\ & + \frac{t}{2} \sum_{i=1}^3 a_i h_i^3(r, s) \left(-\mathbf{V}_2^i \left[\xi_i \alpha_i^\xi \quad \eta_i \alpha_i^\eta \right] \right. \\ & \left. + \mathbf{V}_1^i \left[\xi_i \beta_i^\xi \quad \eta_i \beta_i^\eta \right] \right) \end{aligned} \quad (5a)$$

$$\hat{\mathbf{u}} = \sum_{i=1}^3 h_i^3(r, s) \left[(\xi_i \hat{u}_i^\xi + \eta_i \hat{u}_i^\eta) \mathbf{V}_1^i + (\xi_i \hat{v}_i^\xi + \eta_i \hat{v}_i^\eta) \mathbf{V}_2^i \right] \quad (5b)$$

Further details of the derivation of the displacement interpolation for these shell elements can be found in references (Lee and Bathe 2004, Lee *et al.* 2014, Jeon *et al.* 2014, Jun *et al.* 2018).

With the partition of unity approximation by introducing piecewise polynomials for the nodal displacements, the solution of the MITC3E and MITC3E+ shell elements can be increased without any traditional local mesh refinement. The effectiveness of the method was also reported by evaluating the use of the enrichment scheme applied only locally through the solution of problems (Jeon *et al.* 2014). However, due to the use of the polynomials as a local approximation, the linear dependence problem arises and the global matrix becomes singular. That is a common occurrence which widely exists in various partition-of-unity based methods (Babuska and Melenk 1996, Melenk and Babuska 1996, Duarte and Oden 1996, Oden *et al.* 1998, Strouboulis *et al.* 2000a, b, Duarte *et al.* 2001, Kim and Lee 2018). For the MITC3E and MITC3E+ finite elements, the simplest remedy was adopted by suppressing the higher-order degrees of freedom at the Dirichlet boundary (Jeon *et al.* 2014, Jun *et al.* 2018, Kim and Bathe 2013, Tian *et al.* 2006).

The advantage of the MITC3+ and MITC3E+ shell elements is that the degrees of freedom corresponding to the bubble function can be condensed out at the element level to reduce the computational expense for solving linear equations.

2.2 Assumed covariant transverse shear strain fields

To alleviate the shear locking phenomenon, the unique MITC methods for MITC3, MITC6 and MITC3+ shell

Table 2 Tying positions for the assumed covariant strain of the MITC triangular shell elements. $a=1/2$, $b=1/2$, $c=1/\sqrt{3}$, and $d=1/10,000$ are used (Lee and Bathe 2004, Lee *et al.* 2014, Jeon *et al.* 2014, Jun *et al.* 2018)

Elements	Tying points	r	s	Elements	Tying points	r	s
MITC3	(A3)	a	0		(D6) ₁	$a-b$	0
-	(B3)	0	a	MITC6	(D6) ₂	$a+b$	0
Fig. 2(a)	(C3)	a	a	or	(E6) ₁	0	$a-b$
	(A6) ₁	$a-b$	0	MITC3E	(E6) ₂	0	$a+b$
	(A6) ₂	$a+b$	0	-	(F6) ₁	$a+b$	$a-b$
	(A6) ₃	$a-b$	c	Fig. 2(c)	(F6) ₂	$a-b$	$a+b$
	(B6) ₁	0	$a-b$		(G6)	1/3	1/3
MITC6	(B6) ₂	0	$a+b$		(A4)	1/6	2/3
-	(B6) ₃	c	$a-b$	MITC3+	(B4)	2/3	1/6
Fig. 2(b)	(C6) ₁	$a+b$	$a-b$	or	(C4)	1/6	1/6
	(C6) ₂	$a-b$	$a+b$	MITC3E+	(D4)	1/3+ d	1/3-2 d
	(C6) ₃	$a-b$	$a-b$	-	(E4)	1/3-2 d	1/3+ d
				Fig. 2(d)	(F4)	1/3+ d	1/3+ d

elements are suggested in references (Lee and Bathe 2004, Lee *et al.* 2014, Jeon *et al.* 2014, Jun *et al.* 2018). The important thing to note here is that the covariant membrane strains of the MITC6 shell element are assumed to reduce membrane locking. However, this treatment is not necessary for all 3-node shell elements due to its flat geometry. In this section, we briefly review the MITC schemes for all the triangular shell elements we considered.

We first consider the linear part of the Green-Lagrange strain tensor and its covariant strain components are obtained by

$$e_{ij} = \frac{1}{2}(\mathbf{g}_i \cdot \mathbf{u}_{,j} + \mathbf{g}_j \cdot \mathbf{u}_{,i}), \quad (6a)$$

$$\mathbf{g}_i = \frac{\partial \mathbf{x}}{\partial r_i} \quad \text{and} \quad \mathbf{u}_{,i} = \frac{\partial \mathbf{u}}{\partial r_i} \quad (6b)$$

with $r_1 = r$, $r_2 = s$ and $r_3 = t$.

2.2.1 Assumed strain fields for the MITC3 shell element

The displacement and rotations are interpolated as usual, but for the transverse shear strains, we assume the covariant components are measured in their natural coordinate system. The assumed covariant transverse shear strain field for the MITC3 shell element was introduced in the reference (Lee and Bathe 2004) and can be written by

$$e_{rr}^{\text{AS}} = e_{rr}^{(\text{A3})} + cs \quad \text{and} \quad (7)$$

$$e_{st}^{\text{AS}} = e_{st}^{(\text{B3})} - cr,$$

where $c = e_{st}^{(\text{B3})} - e_{rr}^{(\text{A3})} - e_{st}^{(\text{C3})} + e_{rr}^{(\text{C3})}$ and, at the tying points, $e_{rr}^{(n)}$ and $e_{st}^{(n)}$ are calculated from Eq. (6a). The tying points (A3), (B3), and (C3) are presented in Fig. 2(a) and

Table 2.

2.2.2 Assumed strain fields for the MITC6 shell element

We remark again, that the MITC method for the 6-node shell element was formulated by the use of both assumed membrane and transverse shear strains (Lee and Bathe 2004). The complete in-plane strain field is usually given by two normal shear strains (e_{rr} and e_{ss}) and one in-plane shear strain (e_{rs}). To construct the isotropic in-plane strain field, the normal strain, e_{qq} was introduced in the hypotenuse direction of the right-angled triangle in the natural coordinate system. The in-plane shear strain, e_{rr} was obtained by the following equation.

$$e_{rs}^{\text{AS}} = \frac{1}{2}(e_{rr}^{\text{AS}} + e_{ss}^{\text{AS}}) - e_{qq}^{\text{AS}}. \quad (8)$$

The interpolations of the three in-plane strains (e_{rr} , e_{ss} and e_{qq}) was obtained, as

$$e_{rr}^{\text{AS}} = a_1 + b_1 r + c_1 s, \quad (9a)$$

$$e_{ss}^{\text{AS}} = a_2 + b_2 r + c_2 s, \quad (9b)$$

$$e_{qq}^{\text{AS}} = a_3 + b_3 r + c_3 (1-r-s), \quad (9c)$$

where

$$a_3 = m_{qq}^{(\text{C6})} - l_{qq}^{(\text{C6})}, \quad b_3 = -2l_{qq}^{(\text{C6})}, \quad c_3 = \sqrt{3}(e_{qq}^{(\text{C6})} - a_3 - b_3 r_1), \quad (9f)$$

$$m_{ij}^{(i)} = \frac{1}{2}(e_{ij}^{(i)1} + e_{ij}^{(i)2}), \quad l_{ij}^{(i)} = \frac{\sqrt{3}}{2}(e_{ij}^{(i)2} - e_{ij}^{(i)1}) \quad (9g)$$

with $j = r, s, q$ for $i = \text{A6, B6, C6}$.

The tying positions $(A6)_k$, $(B6)_k$, and $(C6)_k$ with $k = 1, 2, 3$ are presented in Fig. 2(b) and Table 2. Thus, using the in-plane strains e_{rr} , e_{ss} and e_{qq} obtained above, the interpolation function for the in-plane shear strain e_{rs}^{AS} can be obtained by given by Eq. (8).

The assumed strain fields for the transverse shear of the MITC6 shell element were also introduced in the same reference (Lee and Bathe 2004) as

$$e_{rt}^{AS} = a_1 + b_1 r + c_1 s + d_1 rs + e_1 r^2 + f_1 s^2 \quad \text{and} \quad (10a)$$

$$e_{st}^{AS} = a_2 + b_2 r + c_2 s + d_2 rs + e_2 r^2 + f_2 s^2 \quad (10b)$$

with

$$a_1 = m_{rt}^{(D6)} - l_{rt}^{(D6)}, \quad b_1 = 2l_{rt}^{(D6)}, \quad e_1 = 0, \quad (10c)$$

$$a_2 = m_{st}^{(E6)} - l_{st}^{(E6)}, \quad c_2 = 2l_{st}^{(E6)}, \quad f_2 = 0, \quad (10d)$$

$$c_1 = 6e_{rt}^{(G6)} - 3e_{st}^{(G6)} + 2m_{st}^{(F6)} - 2m_{rt}^{(F6)} - 4a_1 - b_1 + a_2, \quad (10f)$$

$$e_2 = 3e_{rt}^{(G6)} - 6e_{st}^{(G6)} + 3m_{st}^{(F6)} - l_{st}^{(F6)} - 3m_{rt}^{(F6)} + l_{rt}^{(F6)} + b_1 + 3a_2 + c_2, \quad (10e)$$

$$f_1 = -6e_{rt}^{(G6)} + 3e_{st}^{(G6)} - 3m_{st}^{(F6)} - l_{st}^{(F6)} + 3m_{rt}^{(F6)} + l_{rt}^{(F6)} + 3a_1 + b_1 + c_2, \quad (10g)$$

$$d_1 = -e_2, \quad d_2 = -f_1, \quad (10h)$$

where

$$m_{jt}^{(i)} = \frac{1}{2}(e_{jt}^{(i_1)} + e_{jt}^{(i_2)}), \quad l_{jt}^{(i)} = \frac{\sqrt{3}}{2}(e_{jt}^{(i_2)} - e_{jt}^{(i_1)}) \quad (10i)$$

with $j = r, s$ for $i = D6, E6, F6$.

The tying positions $(D6)_1$, $(D6)_2$, $(E6)_1$, $(E6)_2$, $(F6)_1$, $(F6)_2$ and $(G6)$ are also presented in Fig. 2(c) and Table 2.

In certain shell problems, the solution using the MITC6 shell element given here obverted the peculiar unstable behaviors, which is reported in references (Chapelle and Suarez 2008). To solve the unstable behaviors, Kim and Bathe (2009) improved the MITC6 shell element with the same membrane strain and transverse shear strain interpolations presented here, but interpolating covariant strain components referred to an element constant contravariant basis.

2.2.3 Assumed strain fields for the MITC3+ shell element

The assumed transverse shear strain fields of the MITC3+ shell element was developed and given by (Lee *et al.* 2014)

$$e_{rt}^{AS} = \frac{2}{3}\left(e_{rt}^{(B4)} - \frac{1}{2}e_{st}^{(B4)}\right) + \frac{1}{3}\left(e_{rt}^{(C4)} + \frac{1}{2}e_{st}^{(C4)}\right) + \frac{1}{3}\hat{c}(3s-1), \quad (11a)$$

$$e_{st}^{AS} = \frac{2}{3}\left(e_{st}^{(A4)} - \frac{1}{2}e_{rt}^{(A4)}\right) + \frac{1}{3}\left(e_{rt}^{(C4)} + \frac{1}{2}e_{st}^{(C4)}\right) + \frac{1}{3}\hat{c}(1-3r), \quad (11b)$$

where $\hat{c} = e_{rt}^{(F4)} - e_{rt}^{(D4)} - e_{st}^{(F4)} + e_{st}^{(E4)}$ and the tying positions $(A4)$, $(B4)$, $(C4)$, $(D4)$, $(E4)$, and $(F4)$ are presented in Fig. 2(d) and Table 2. The in-plane covariant strain components for the MITC3+ shell element are directly obtained from Eq. (6a).

2.2.4 Assumed strain fields for the MITC and MITC3+ shell elements

Since displacement interpolations for the MITC3E and MITC3E+ shell elements can be split into two parts, linear and quadratic terms, the covariant strain components are directly separated into two parts as well,

$$e_{ij} = \bar{e}_{ij} + \hat{e}_{ij} \quad (12a)$$

$$\text{with } \bar{e}_{ij} = \frac{1}{2}(\mathbf{g}_i \cdot \bar{\mathbf{u}}_{,j} + \mathbf{g}_j \cdot \bar{\mathbf{u}}_{,i}) \quad \text{and} \quad (12b)$$

$$\hat{e}_{ij} = \frac{1}{2}(\mathbf{g}_i \cdot \hat{\mathbf{u}}_{,j} + \mathbf{g}_j \cdot \hat{\mathbf{u}}_{,i}),$$

in which \bar{e}_{ij} and \hat{e}_{ij} correspond to the standard linear and additional quadratic displacement interpolations, respectively. The covariant strains components, \bar{e}_{ij} and \hat{e}_{ij} for the MITC3E shell element were replaced with the assumed covariant transverse shear strain fields developed for the MITC3 and MITC6b (Lee and Bathe 2004) shell elements, respectively, in order to alleviate share locking (Jeon *et al.* 2014). Thus, the assumed covariant transverse shear strain related to the quadratic displacement interpolation is

$$\hat{e}_{rt}^{AS} = a_1 + b_1 r + c_1 s, \quad (13a)$$

$$\hat{e}_{st}^{AS} = a_2 + b_2 r + c_2 s, \quad (13b)$$

and we have the coefficients,

$$a_1 = m_{rt}^{(H6)} - l_{rt}^{(H6)}, \quad b_1 = 2l_{rt}^{(H6)}, \quad (13c)$$

$$a_2 = m_{st}^{(I6)} - l_{st}^{(I6)}, \quad c_2 = 2l_{st}^{(I6)},$$

$$c_1 = (a_2 + c_2 - a_1) - (m_{st}^{(J6)} + l_{st}^{(J6)} - m_{rt}^{(J6)} - l_{rt}^{(J6)}), \quad (13d)$$

$$b_2 = (a_1 + b_1 - a_2) + (m_{st}^{(J6)} - l_{st}^{(J6)} - m_{rt}^{(J6)} + l_{rt}^{(J6)}) \quad (13c)$$

$$\text{with } m_{jt}^{(i)} = \frac{1}{2}(\hat{e}_{jt}^{(i_1)} + \hat{e}_{jt}^{(i_2)}), \quad l_{jt}^{(i)} = \frac{\sqrt{3}}{2}(\hat{e}_{jt}^{(i_2)} - \hat{e}_{jt}^{(i_1)}) \quad (13e)$$

with $j = r, s$ for $i = H6, I6, J6$,

where the tying positions $(D6)_k$, $(E6)_k$, $(F6)_k$, with $k = 1, 2$ are presented in Fig. 2(c) and Table 2.

Since the enriched displacement $\hat{\mathbf{u}}$ for the MITC3E+ shell element is not affecting the transverse shear strains,

Table 3 The number of non-zero entries of the stiffness matrix and solution times (in seconds) for Scordelis-Lo Roof problem shown in Fig. 25(a). The solution times are obtained using the 100×100 element mesh with the mesh pattern I given in Fig. 25(b) (DOFs: degrees of freedom)

Element type	Total DOFs	Half-bandwidth	Skyline storage (COMSOL)		Compressed row storage (PARDISO)	
			# of non-zero entries	Time	# of non-zero entries	Time
MITC3	50,400	513	25,516,887	4.09	894,494	0.92
MITC6	200,800	2,021	302,564,176	178.25	5,821,203	4.81
MITC3+	90,400	921	82,262,731	22.67	1,550,896	1.61
MITC3E	151,200	1,539	229,500,783	140.34	7,899,246	7.56
MITC3E+	130,000	1,329	170,691,847	84.16	3,968,832	3.55

the assumed transverse shear strain fields (Eq. (11a) and (11b)) used in the MITC3+ shell element were directly adopted (Jun *et al.* 2018). Again, the in-plane covariant strain components for the MITC3E and MITC3E+ shell elements are directly obtained from Eq. (12a).

3. Computational efficiency

In this section, we investigate some important aspects of the computational efficiency when using the MITC triangular shell elements. To precisely compare the computational cost, we first analyze the size (the number of total degrees of freedom) and sparseness of the global stiffness matrices. With the same triangular mesh pattern, the square domain discretized by 6×6 element meshes are considered in Fig. 3(a) for the 3-node elements and Fig. 3(b) for the 6-node element.

The stiffness matrices for the general shell problem, without imposing boundary conditions, are plotted in Fig. 3(c)-(g), where the non-zero entries are presented with colored squares. In each panel, the size of the matrix (the number of total degrees of freedom) and the number of non-zero entries and half-bandwidth corresponding to matrix are numbered. It is interesting that the number of non-zero entries in the global stiffness matrix for the MITC3E shell element is substantially larger than in the corresponding matrix for the MITC6 shell element. This is due to the fact that the support of the higher order interpolation functions in the MITC3E shell element is larger than for other elements. However, using the MITC3E shell element, all degrees of freedom are associated with vertex nodes which are shared by several elements. The assembled system of equations is in general smaller than when using the MITC6 shell element where edge nodes are only shared by two elements. Therefore, the MITC3E shell element has fewer equations and a smaller bandwidth than the MITC6 shell element. This fact reflects the different computational efficiency depending on the matrix storage format used. When using the skyline solver, the MITC3E shell element is more efficient than the MITC6 shell element due to its smaller bandwidth (see Fig. 4(a)). However, when the Compressed Row Storage (CRS) which does not store any unnecessary elements is used, the MITC3E shell element is computationally more expensive than the MITC6 shell element (see Fig. 4(b)).

It is valuable to compare solution times required for the five MITC triangular shell elements. Their formulation, of course, leads to symmetric stiffness matrices. The computations are performed by Intel Fortran XE 2017 on Intel Core i7-4770 CPU @ 3.40 GHz, 24GB RAM, 64-bit Windows 10 operating system. Additionally, all solutions using the MITC3 and MITC6 shell elements are validated with the commercial finite element software, ADINA version 9.0. We first focus our attention to the solution times using the MITC3 shell element with two different linear equation solvers; Skyline solver (COLSOL and SKYSOL (Bathe 2016) and sparse direct solver (MUMPS and PARDISO (Karypis and Kumar 1998, Schenk and Gartner 2006), see Fig. 4(c). The computational costs of five MITC shell elements are presented in Fig. 4(d) and listed in Table 3 using Skyline solver, SKYSOL and sparse direct solver, PARDISO. As expected, the solution time for the MITC3E shell element is much smaller than that for the MITC6 shell element when the skyline solver is used. On the contrary, when using the sparse solver, PARDISO, the solution time for the MITC6 shell element is much more efficient than one for the MITC3E shell element.

4. Benchmark problems

In this section, a summary of the results obtained in the assessments and comparisons of MITC triangular shell elements in the linear range are presented. Twelve popular benchmark problems are considered, including four plane stress and two plate problems to evaluate the performance of membrane and bending behaviors when applying either a partition of unity approximation or a bubble node, or both into 3-node shell element. The plane stress condition is achieved by imposing $w=\alpha=\beta=0$ for all nodes of the shell finite element and the solutions of the MITC3+ and MITC3E+ elements are the exactly identical to those of the MITC3 and MITC3E elements, respectively. In plate problems by imposing $u=v=0$, the MITC3+ element has the same solution accuracy of the MITC3E+ element. In each example, the reference solutions are provided by either analytical solutions or literatures.

4.1 Mesh distortion test using the cantilever beam

The cantilever beam to test distortion sensitivity is

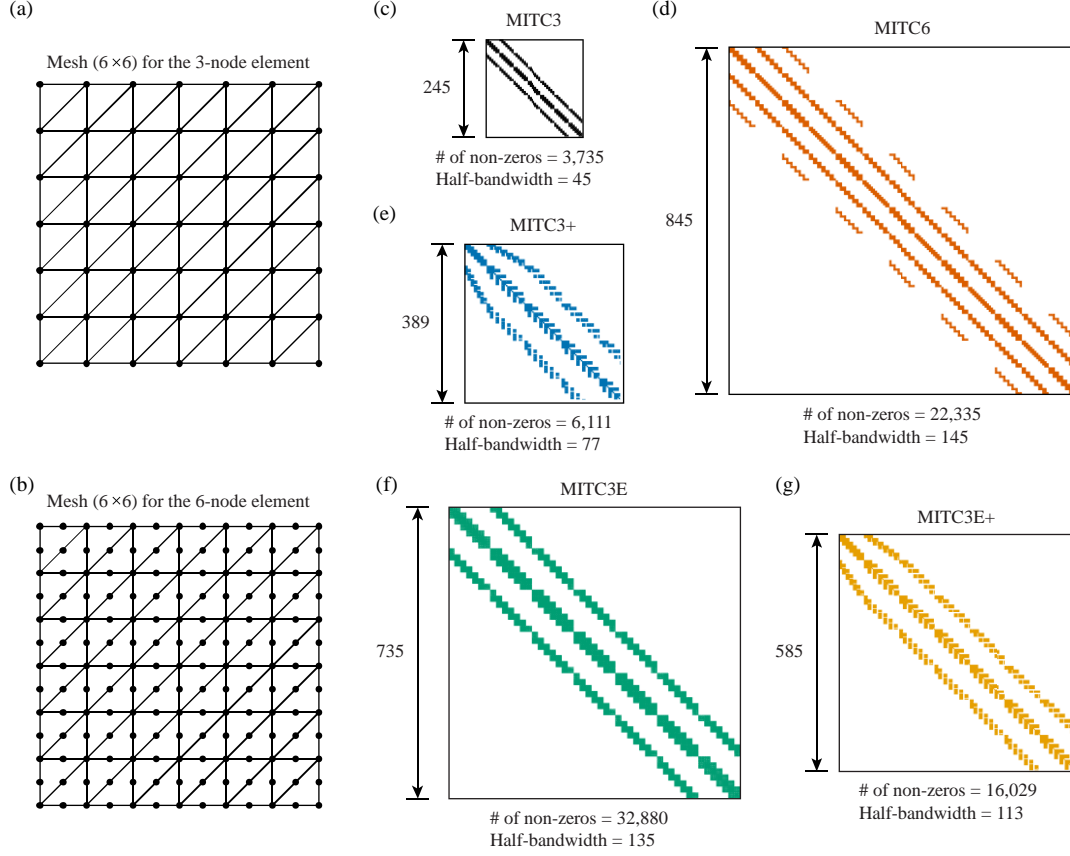


Fig. 3 Mesh used and stiffness matrix structures: 6×6 element meshes for the (a) 3- and (b) 6-node elements. Global stiffness matrix patterns for the (c) MITC3, (d) MITC6, (e) MITC3+, (f) MITC3E, and (g) MITC3E+ shell elements for the general shell problem without imposing the boundary conditions. Non-zero entries are colored in the stiffness matrix structure. All matrices are symmetric, thus only upper triangular portion of each matrix is stored

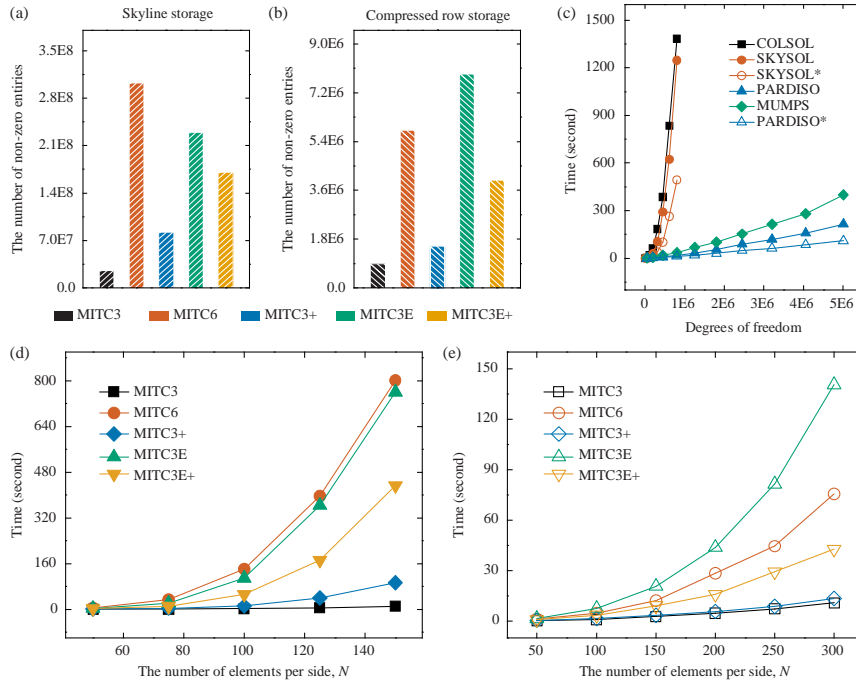


Fig. 4 Comparisons of the computational efficiency for the MITC triangular shell elements when considering the Scordelis-Lo roof shell problem shown in Fig. 25(a). The total number of non-zero entries of the stiffness matrix when the (a) skyline and (b) compressed row storage are used. The solution times for solving linear equations (c) using different linear equation solvers, and for different shell elements with the (d) COLSOL and (e) PARDISO solvers. (*) indicates the solver with the single-precision floating points)

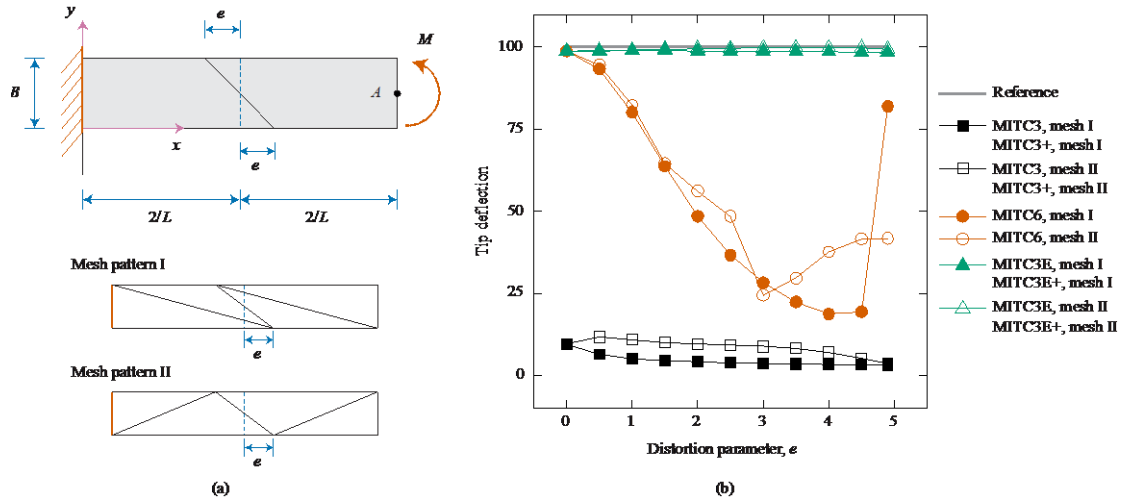


Fig. 5 Cantilever beam divided by two elements with distorted parameter, e : (a) Problem description ($L=10$, $B=2$, thickness $h=1$, $M=2,000$, $E=1,500$ and $\nu=0.25$) and mesh patterns used (1×2), (b) Results of the tip deflection at point A of the beam

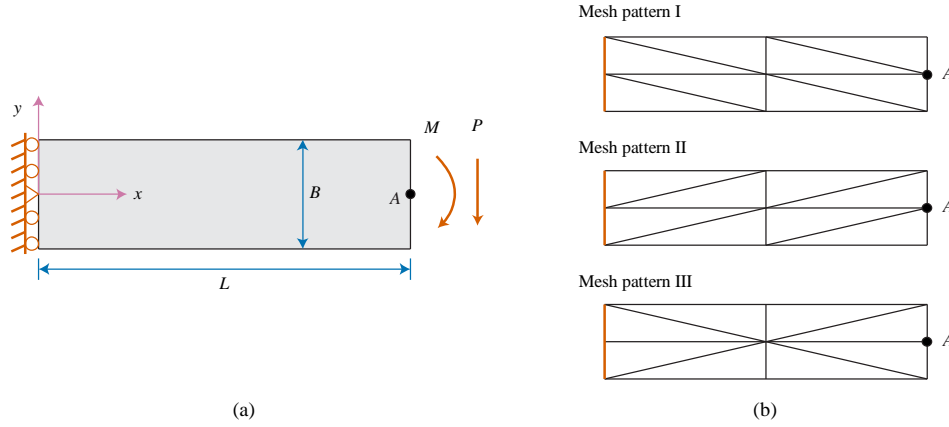


Fig. 6 A cantilever beam subjected to tip shear force or moment; (a) Problem description ($L=48$, $B=12$, thickness $h=1$, $M=24,000$, $P=1,000$, $E=3.0 \times 10^7$ and $\nu=0.3$). (b) Mesh patterns I, II and III used ($N=2$)

discretized by two elements under plane stress condition, as shown in Fig. 5(a). The shape of the two elements varies with the distorted parameter e , which reflects the degree of element distortion. The cantilever beam has the geometry of length $L=10$, width $B=2$ and thickness $h=1$, its Young's modulus $E=1,500$ and the Poisson ratio $\nu=0.25$. The moment $M=2,000$ is applied at the free end. The exact solution for the case is given by Timoskenko (1970) and Xu and Rajendran (2013) as below

$$v = -\frac{\nu M}{2EI} y^2 - \frac{M}{2EI} x^2, \quad (14)$$

where I is the second moment of area of the beam's cross section.

The results of the tip deflection at point A are presented in Fig. 5(b). Providing the exact solution when e varies from 0 to 5, the MITC3E element is more robust than other elements, showing that the partition of unity approximation can overcome the trapezoidal locking completely.

4.2 Cantilever beam subjected to tip shear and moment

We consider the cantilever beam (as shown in Fig. 6(a)) subjected to either tip shear or moment. The numerical values for this problem are as follows: $L=48$ and $B=12$, thickness $h=1$, $M=24,000$ for moment and $P=1,000$ for shear force, Young's modulus $E=3.0 \times 10^7$ and Poisson's ratio $\nu=0.3$. The problem is solved with the plane stress condition. Three mesh patterns I, II, and II as shown in Fig. 6(b) are considered.

The solutions are obtained using $N \times N$ element meshes ($N=2, 4, 6, 8, 10, 12$, and 16). The exact solution under moment is calculated by Eq. (14). For the cantilever beam subjected to shear force, the exact solution is obtained as below

$$v = \frac{P}{6EI} \left[3\nu y^2 (L-x) + (4+5\nu) \frac{D^2 x}{4} + (3L-x)x^2 \right] \quad (15)$$

with $D = Eh^3 / 12(1-\nu^2)$.

The convergence of normalized displacement ($v_C = v_{ref}$) at point A is presented in Fig. 7(a) for the tip shear force load case and in Fig. 7(b) for the moment load case. For all cases, the MITC6 and MITC3E elements exhibit almost the

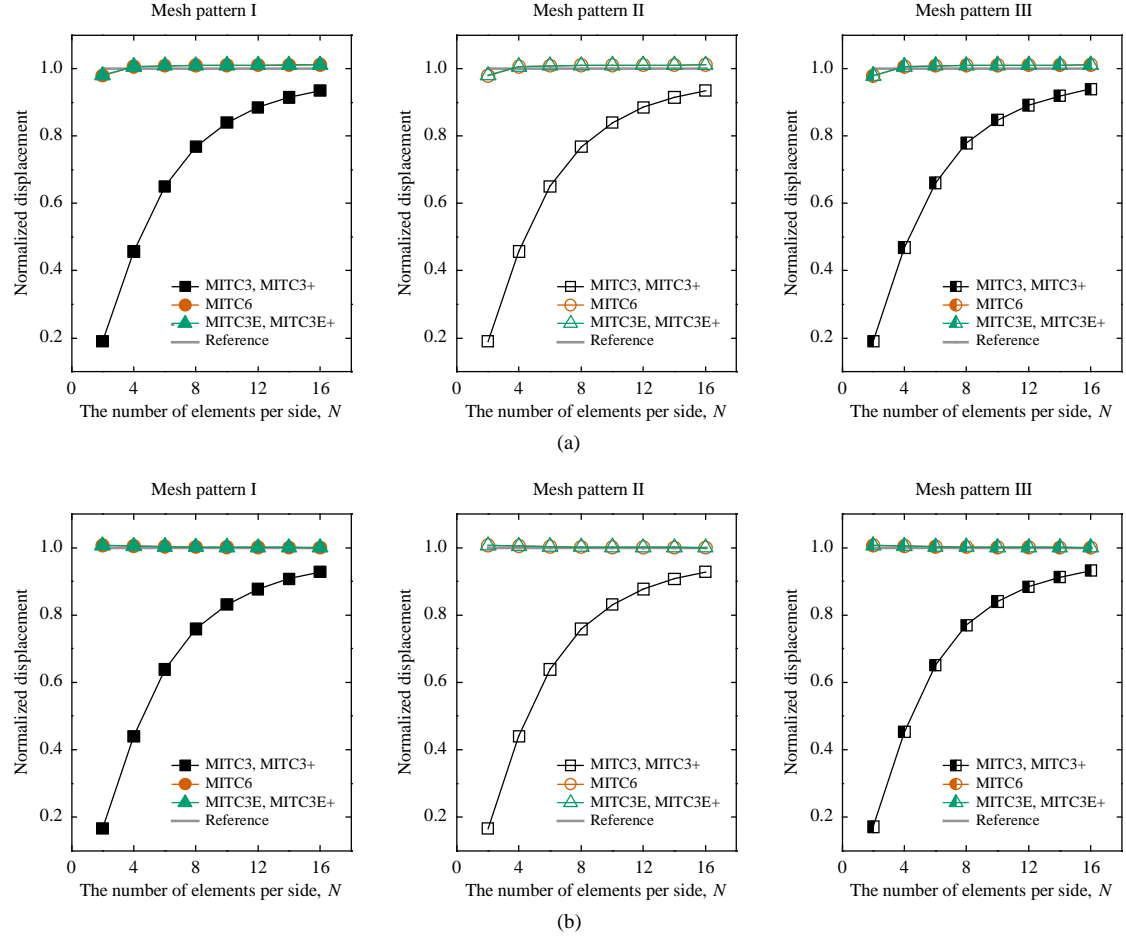


Fig. 7 Convergence of normalized displacement at point A for the cantilever beam subjected to (a) tip shear force and (b) moment

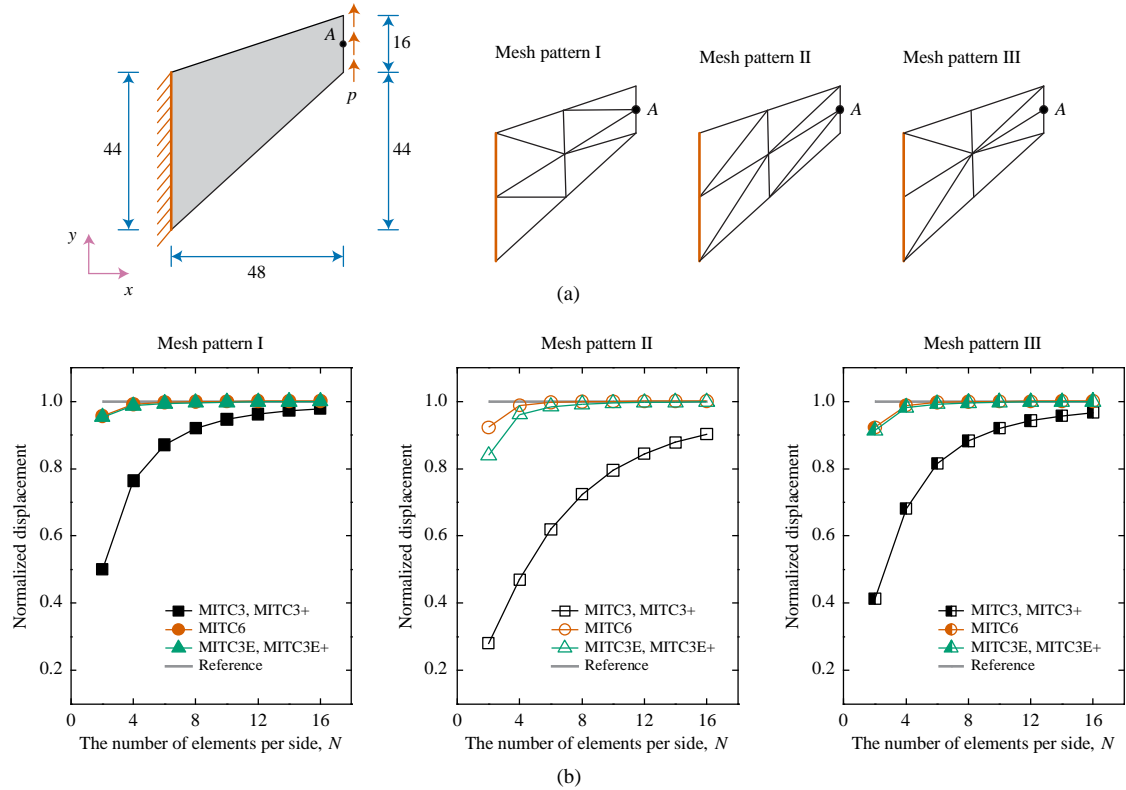


Fig. 8 Cook's skew beam problem. (a) Problem description (thickness $h=1$, $p=1/16$, $E=1$ and $\nu=1/3$) and mesh patterns I, II, and III used ($N=2$). (b) Convergence of normalized displacement at point A for the skew beam

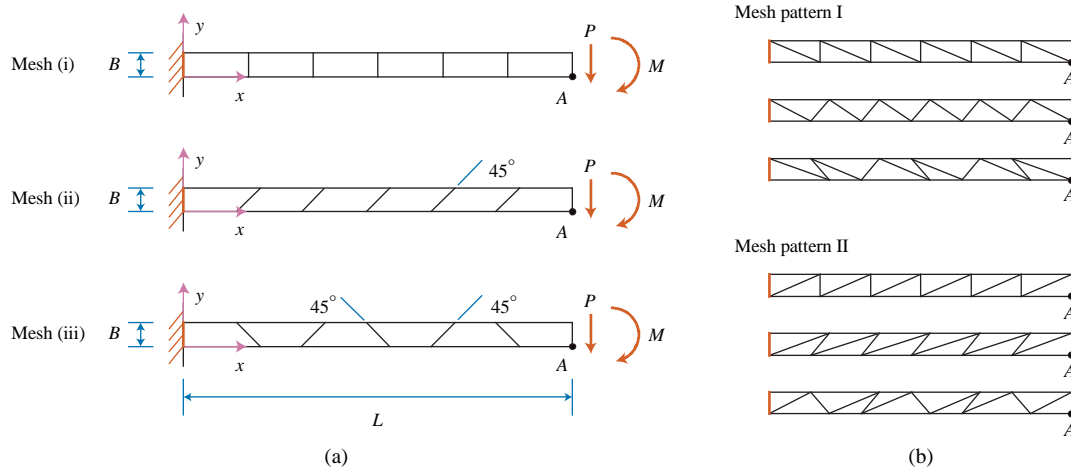


Fig. 9 MacNeal problem subjected to two load cases; Unit tip shear force P and unit tip bending moment M . (a) Problem description ($L=6$, $B=0.2$, thickness $h=0.1$, $P=1$, $M=0.2$, $E=10^7$ and $\nu=0.3$). (b) Mesh patterns I and II used (1×6)

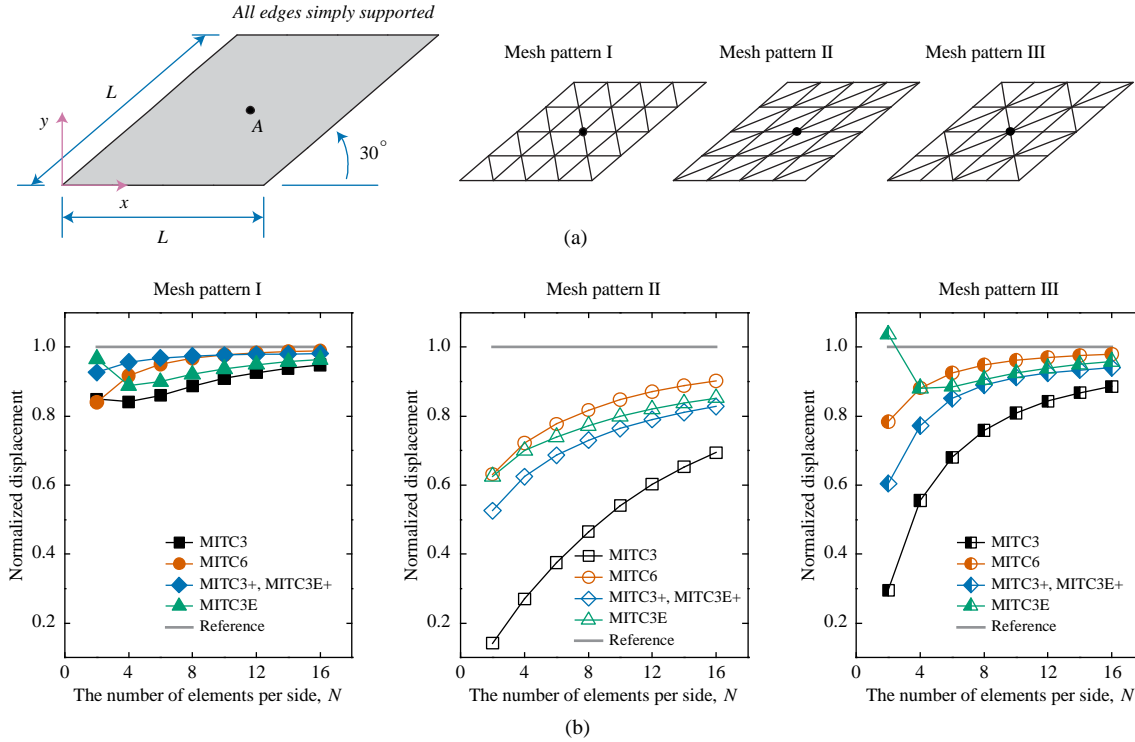


Fig. 10 Morley's 30° skew plate under uniform pressure. (a) Problem description ($L=100$, thickness $h=1$, $E=10^5$, and $\nu=0.3$) and mesh patterns I, II and III used ($N=4$), (b) Convergence of normalized displacement at point A for the skew plate

same results as the exact solution regardless of the mesh density.

4.3 Cook's skew beam

The skew beam problem proposed by Cook *et al.* (2007) is useful to assess the membrane performance of finite elements. The geometric dimensions and boundary conditions used are shown in Fig. 8(a). The material properties are Young's modulus $E=1$ and Poisson's ratio $\nu=1/3$. The beam is subjected to a distributed shear load $p=1/16$ per length at the right end. The problem is solved

under the plane stress condition.

The solutions are obtained using $N \times N$ element meshes ($N=2, 4, 6, 8, 10, 12$, and 16). The reference solution of the vertical displacement at the free-end mid-point A is 23.95 given in reference (Cook *et al.* 2007). Three different mesh patterns I, II, and III shown in Fig. 8(a) are considered.

The convergence of normalized displacement (v_A/v_{ref}) at point A is presented in Fig. 8(b). The MITC6 and MITC3E elements exhibit the good results compared with the exact solution

4.4 MacNeal beam

Table 4 Normalized tip displacements at point A , v_A for the MacNeal's cantilever beam subjected to either unit tip shear force $P=1$ or unit tip moment $M=0.2$

Element type	Load $P=1$			Load $M=0.2$		
	Mesh (i)	Mesh (ii)	Mesh (iii)	Mesh (i)	Mesh (ii)	Mesh (iii)
MITC3, mesh I	0.0316	0.0222	0.0149	0.0311	0.0203	0.0135
MITC3, mesh II	0.0316	0.0113	0.0191	0.0311	0.0093	0.0167
MITC6, mesh I	0.9541	0.8221	0.7648	0.9866	0.8775	0.8044
MITC6, mesh II	0.9541	0.7789	0.8034	0.9866	0.8157	0.8586
MITC3E, mesh I	0.9831	0.9704	0.9610	0.9927	0.9936	0.9924
MITC3E, mesh II	0.9831	0.9704	0.9610	0.9927	0.9936	0.9924

Reference solution v_{ref} (MacNeal and Harder 1985) = -0.1081 for load P and -0.054 for load M . Mesh patterns I and II are shown in Fig. 9(b)

The thin cantilever beam suggested by MacNeal (MacNeal and Harder 1985) has frequently been used as a test problem. The cantilever beam has length $L=6$, width $B=0.2$, and thickness $h=0.1$. The material properties are given by Young's modulus $E=10^7$ and Poisson's ratio $\nu=0.3$. We consider two loading cases; shear force ($P=1$) and moment ($M=0.2$) at the free tip. Three different meshes (rectangular, parallelogram, and trapezoidal shapes) are applied as shown in Fig. 9(a). In addition, two triangular mesh patterns (shown in Fig. 9(b)) are used for the elements compared. The plane stress condition is also considered for this problem.

The solutions are obtained using 1×6 element meshes and the reference value of $v_{ref} = -0.1081$ for the shear load case and $v_{ref} = -0.0054$ for the moment load case (MacNeal and Harder 1985) are used.

Table 4 shows normalized tip displacements at point A ($v_A = v_{ref}$). The results for the element with the partition of unity approximation show high accuracy for all three mesh-types regardless of mesh distortion.

4.5 Morley's 30° skew plate

The Fig. 10(a) shows the skew plate under uniform pressure in the z -direction. Morley (1963) originally proposed the skew plate to test the sensitivity of the plate elements to mesh distortions. The plate is modeled with edges of L and all edges are simple supported. The geometric data and material properties are $L=100$, thickness $h=1$, $E=10^5$ and $\nu=0.3$ which are based on the work of Andelfinger and Ramm (1993). Three mesh patterns I, II, and III shown in Fig. 10(a) are used for the elements being compared. This problem is also solved under the plate problem condition.

The solutions are obtained using $N \times N$ element meshes ($N=2, 4, 6, 8, 10, 12$, and 16). The Kirchhoff reference solution of 4.455 suggested by Morley is replaced by the value 4.640, as even for the length to thickness ratio of 100 shear deformation effects cannot be neglected.

Fig. 10(b) presents convergences of the normalized

Table 5 Normalized displacement at point A for the curved beam shown in Fig. 14(a)

Element type	In-plane loading P_1	Out-of-plane loading P_2
MITC3, mesh I	0.0249	0.6214
MITC3, mesh II	0.0253	0.6278
MITC6, mesh I	0.9777	0.8877
MITC6, mesh II	0.9737	0.8877
MITC3+, mesh I	0.0249	0.7944
MITC3+, mesh II	0.0253	0.7828
MITC3E, mesh I	0.9966	0.9633
MITC3E, mesh II	0.9974	0.9621
MITC3E+, mesh I	0.9966	0.7944
MITC3E+, mesh II	0.9974	0.7828

Reference v_{ref} (MacNeal and Harder 1985) = 0.08734 for load P_1 and -0.50220 for load P_2 . Mesh patterns I and II are shown in Fig. 14(b)

vertical displacement at point A using the MITC3, MITC6, MITC3+, and MITC3E shell elements. The results show that the convergence of all elements is highly sensitive to the mesh patterns.

4.6 Circular plate under uniform pressure

A circular plate loaded with a downward uniform pressure, shown in Fig. 11(a), is analyzed. We consider the plate with either simply supported or fully clamped boundary conditions along its edges. This problem is often used to verify results of new elements since analytical solutions are readily available in this case. The circular plate has a radius $R=1$ and two kinds of thickness $h=0.1$ or $h=0.01$. The material has a Young's modulus of $E=1.7472 \times 10^7$ and Poisson's ratio of $\nu=0.3$. Utilizing symmetry, only one-quarter of the plate corresponding to the shaded region in Fig. 11(a) is modeled. Three mesh patterns I, II, and III shown in Fig. 11(b) are considered. The solutions are obtained using the quadrant shell (shaded region) divided into three regions and each region is discretized using $N \times N$ element meshes (hereafter referred to as $3 \times (N \times N)$ for three regions, each consisting of $N \times N$ and $N=1, 2, 3, 4, 5$, and 6). A simply supported and clamped circular plates are analyzed to demonstrate more features of the triangular elements. Based on the Kirchhoff thin plate theory, the reference displacements at the center of the circular plate (point A) are given as follows (Andelfinger and Ramm 1993)

$$w_{ref} = -\frac{R^4}{64D} \cdot \frac{5+\nu}{1+\nu}$$

for the simply supported boundary,

$$w_{ref} = -\frac{R^4}{64D} \quad \text{for the clamped boundary,} \quad (16a)$$

$$\text{with } D = Eh^3 / 12(1-\nu^2).$$

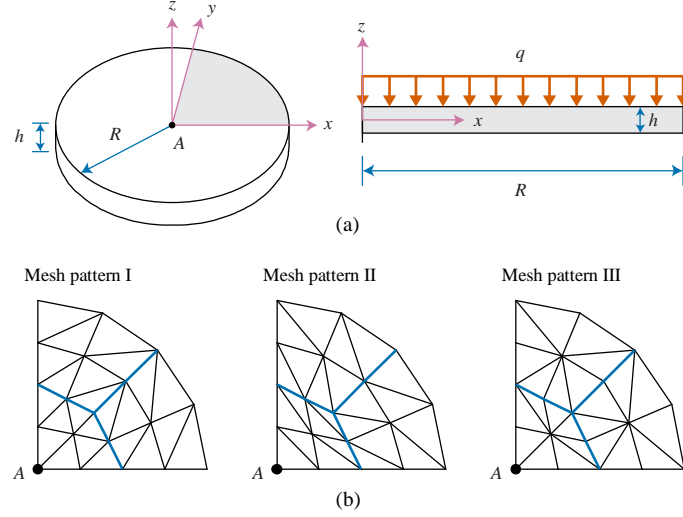


Fig. 11 Circular plate under uniform pressure. (a) Problem description ($R=1$, thickness $h=0.1$ or 0.01 , $q=1$, $E=1.7472 \times 10^7$ and $\nu=0.3$), (b) Mesh patterns I, II, and III used ($N=2$)

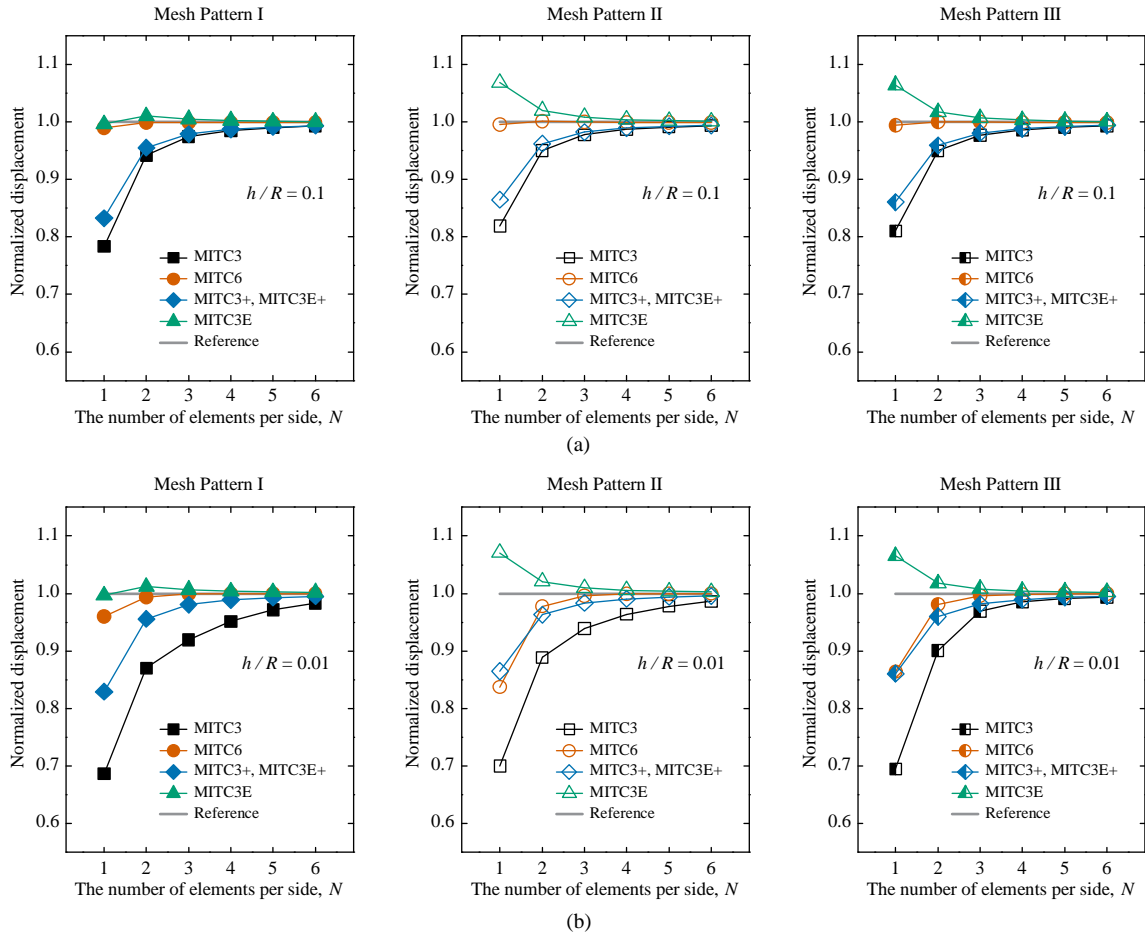


Fig. 12 Convergence of normalized displacement at point A for the simply supported plate with (a) $h/R=0.1$ and (b) $h/R=0.01$

4.7 Curved beam

Figs. 12 and 13 present the convergences of normalized displacement for the simply supported and fully clamped cases, respectively. The MITC6 and MITC3E shell finite elements produce much better solution results than other shell elements even coarse meshes.

The curved beam shown in Fig. 14(a) is clamped at one end and loaded by a unit force at the other. The geometry and material properties are $R_1=4.12$, $R_2=4.32$, thickness $h=0.1$, $E=1 \times 10^7$ and $\nu=0.25$. Two loading conditions are

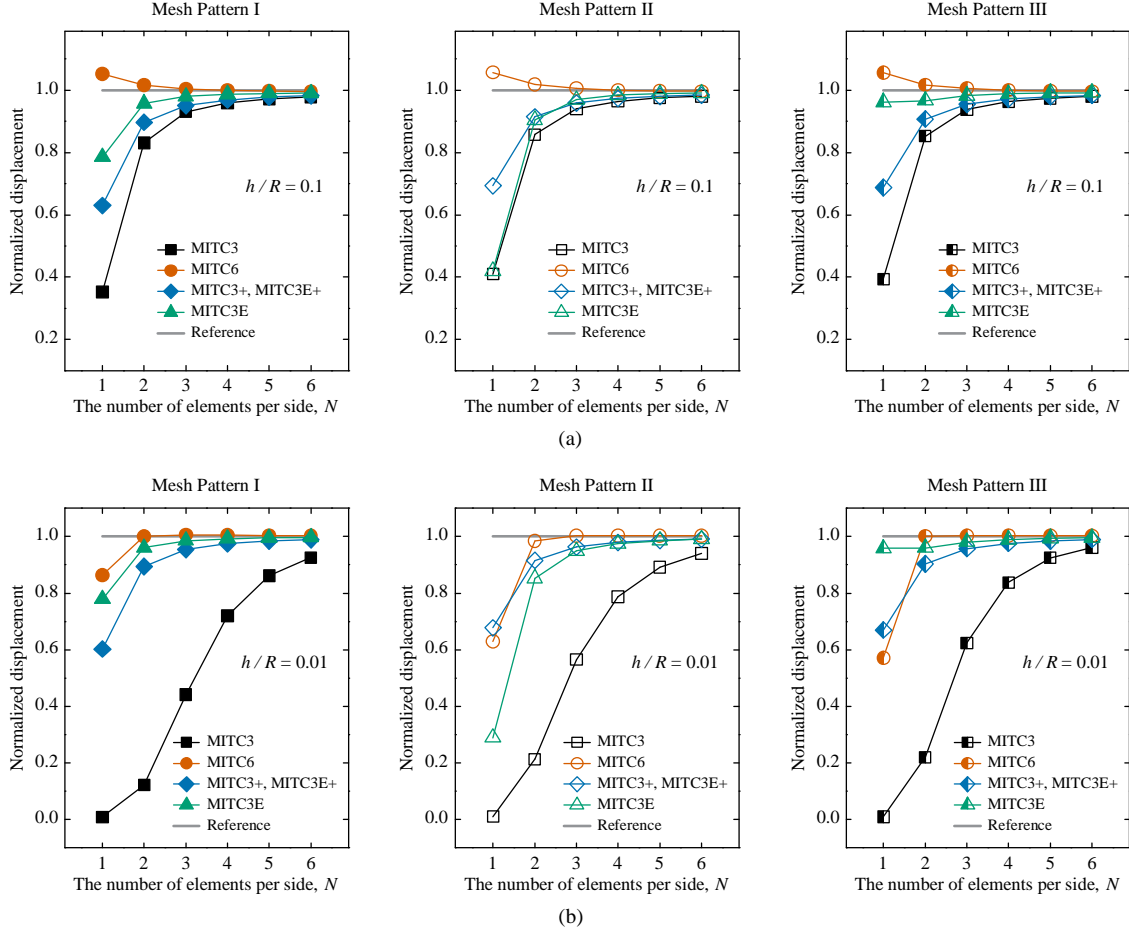


Fig. 13 Convergence of normalized displacement at point A for the fully clamped plate with (a) $h/R=0.1$ and (b) $h/R=0.01$

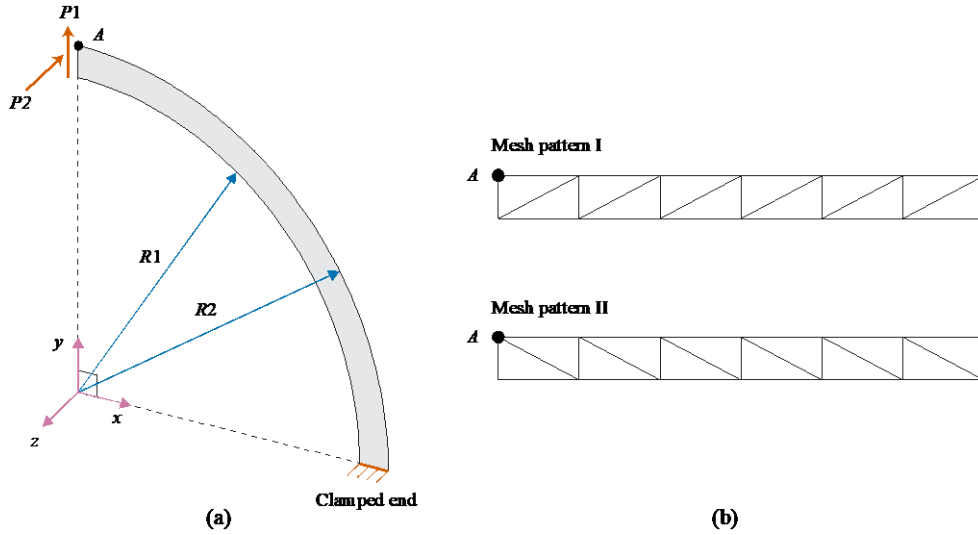


Fig. 14 Curved beam with the in-plane or out-of-plane load cases. (a) Problem description ($R_1=4.12$, $R_2=4.32$, thickness $h=0.1$, $P_1=1$, $P_2=1$, $E=1 \times 10^7$ and $\nu=0.25$). (b) Mesh patterns I and II used (1×6)

considered along the in-plane axis $P_1=1$ and the out-of-plane axis $P_2=1$. Two triangular mesh patterns I and II shown in Fig. 14(b) are considered. The solutions are obtained using the 1×6 element mesh. The displacements at the free end in the directions of the forces are computed and normalized by the reference solution of MacNeal and Harder (MacNeal and Harder 1985); $v_{ref}=0.08734$ under in-

plane load case and $w_{ref}=-0.5022$ under out-of-plane load case.

Table 5 lists two normalized displacements (v_A/v_{ref} and w_A/w_{ref}) at point A for the in-plane and out-of-plane load cases, respectively. The best performance is obtained with the MITC3E shell element under both loading cases.

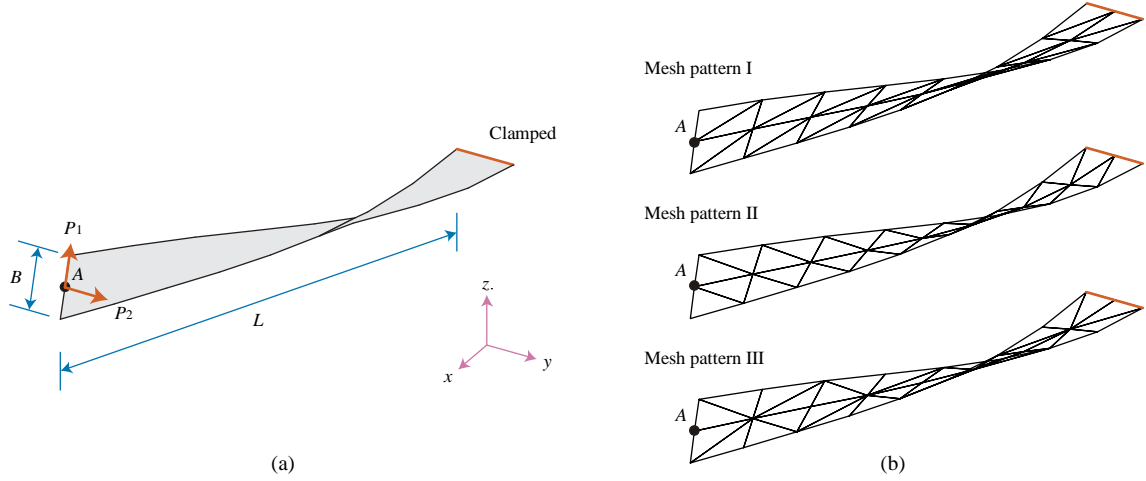


Fig. 15 Twisted beam with two different loading conditions; in-plane and out-of-plane load cases. (a) Problem description ($L=12$, $B=1.1$, thickness $h=0.32$ and 0.0032 , $P_1=1$, $P_2=1$, $E=29 \times 10^6$ and $\nu=0.22$). (b) Mesh patterns I, II and III used (2×8)

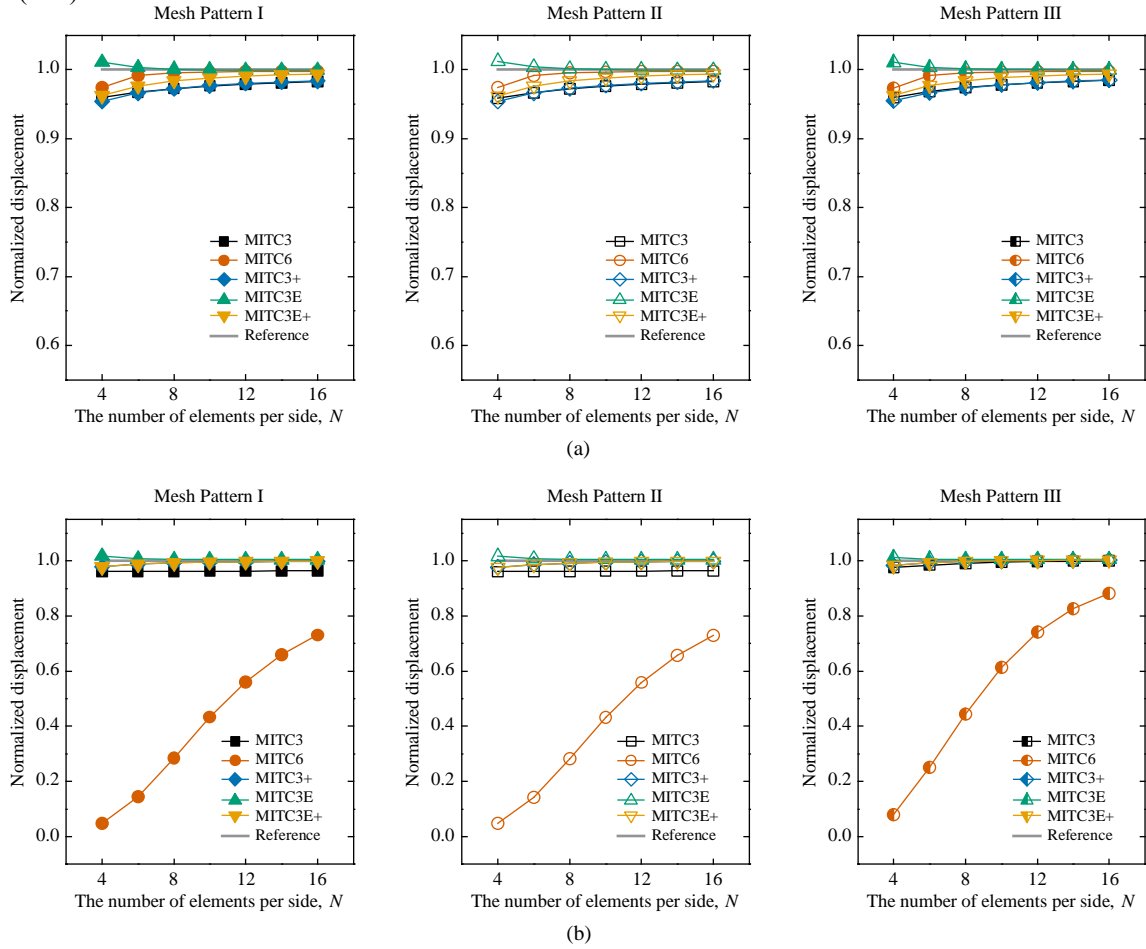


Fig. 16 Convergence of normalized displacement at point A for the twisted beam with the thickness of (a) 0.32 and (b) 0.032 under in-plane load

4.8 Twisted beam

The twisted beam problem shown in Fig. 15(a) was introduced in references (MacNeal and Harder 1985, Belytschko *et al.* 1989) to test the effect of element warping. The initial geometry of the beam is twisted, but the initial strain is zero. The geometric and material

properties are $L=12$, $B=1.1$, Young's modulus $E=29 \times 10^6$, and Poisson's ratio $\nu=0.22$. The initially twisted beam is fully clamped at one end and is loaded by a point load at the center of the free tip (point A). Two load cases are considered; an in-plane load $P_1=1$ and an out-of-plane load $P_2=1$. Three mesh patterns I, II, and III shown in Fig. 15(b) are considered.

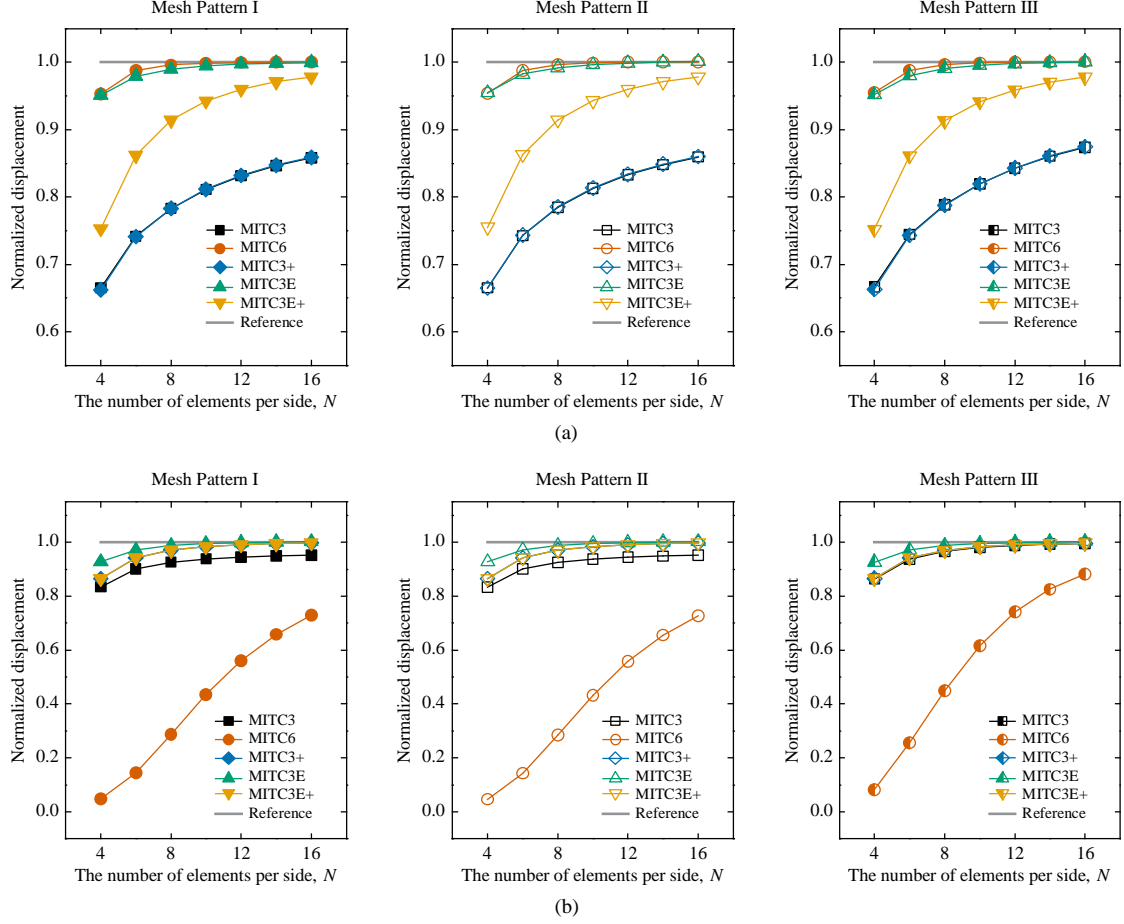


Fig. 17 Convergence of normalized displacement at point A for the twisted beam with the thickness of (a) 0.32 and (b) 0.032 under out-of-plane load

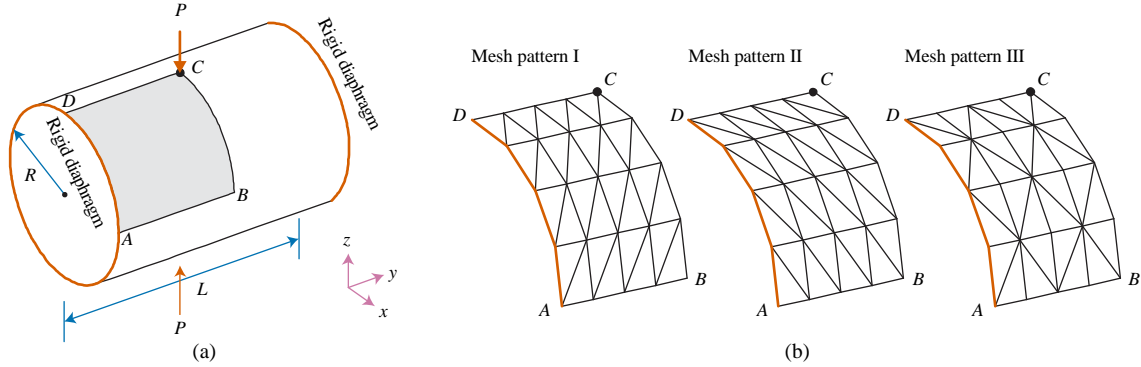


Fig. 18 Pinched cylinder problem. Problem description ($L=600$, $R=300$, thickness $h=3$, $P=1.0$, $E=3 \times 10^6$ and $\nu=0.3$). (b) Mesh patterns I, II and III used ($N=4$)

The solutions are obtained using $2 \times N$ element meshes ($N=4, 6, 8, 10, 12, 14$, and 16). The performance of shell elements of two kind of thickness ($h=0.32$ and $h=0.0032$) was studied under in-plane and out-of-plane loads. When $h=0.32$, the reference displacements at point A are $w_{ref}=5.424 \times 10^3$ and $v_{ref}=1.754 \times 10^3$ for the in-plane and out-of-plane load cases, respectively. When $h=0.0032$, the reference displacements are $w_{ref}=5.256 \times 10^3$ and $v_{ref}=1.29 \times 10^3$ for the in-plane and out-of-plane load cases, respectively (MacNeal and Harder 1985, Belytschko *et al.* 1989).

Figs. 16 and 17 show the convergence of two normalized displacements (w_A/w_{ref} and v_A/v_{ref}) at the tip center for the in-plane and out-of-plane load cases, respectively. In case of the beam with thickness of 0.32, all considered elements perform well when uniform mesh is used. With distorted meshes, the solution of the MITC6 shell element is significantly deteriorated. When the beam with the thickness of 0.0032 is modeled using uniform meshes, the MITC3 and MITC3+ shell elements do not show good convergence behavior even using the finer element meshes. Again, regardless of the mesh patterns, all

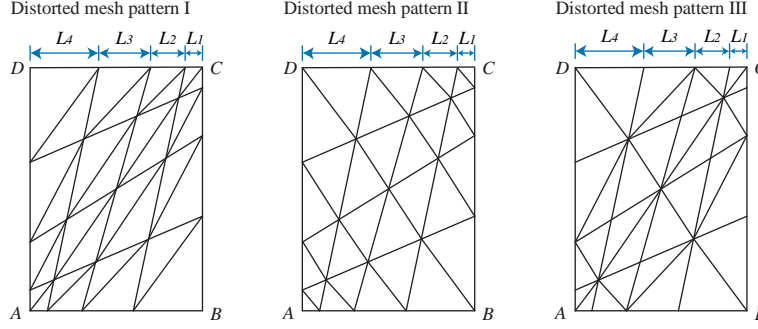


Fig. 19 Three distorted mesh patterns for the numerical problems solved when $N=4$

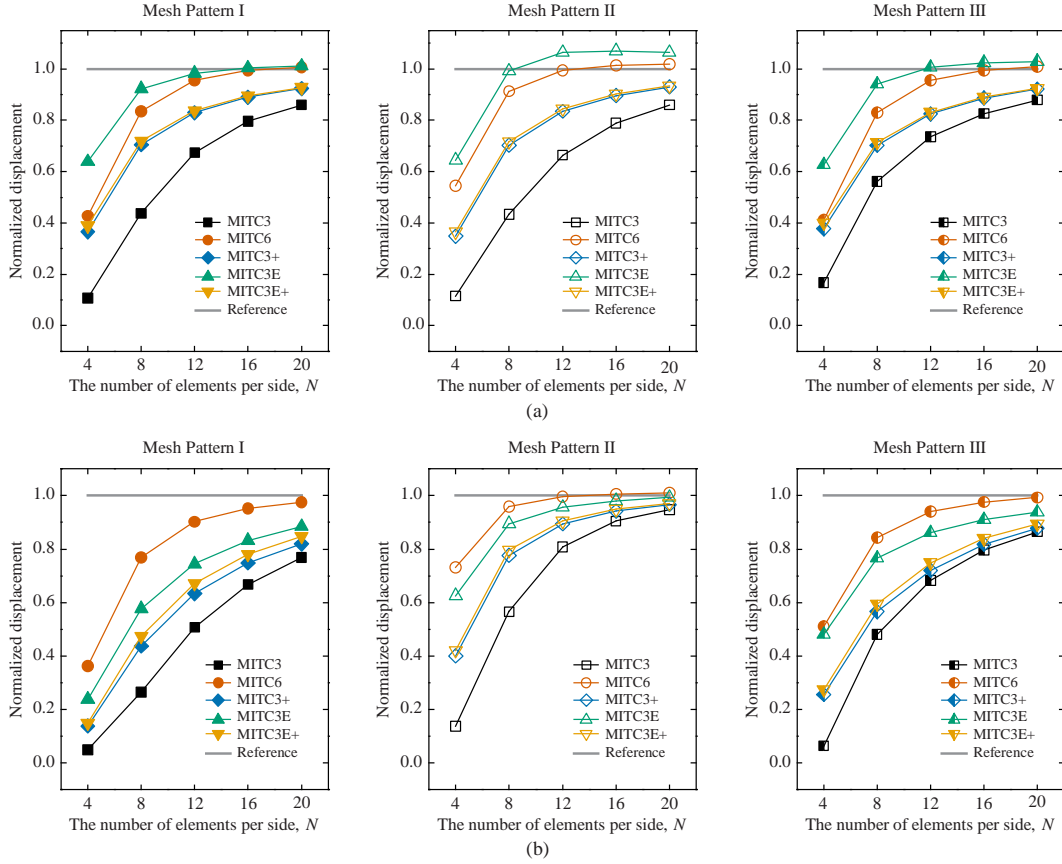


Fig. 20 Convergence of normalized displacement at point C for the pinched cylinder with (a) uniform and (b) distorted meshes shown in Fig. 19

solutions of the MITC6 shell element with distorted meshes are severely distorted, even though others show excellent solutions.

4.9 Pinched cylinder

Fig. 18(a) illustrates a short cylinder subjected to two pinching forces. The shell is bounded by rigid diaphragms at each end. This pinched cylinder is one of the most severe benchmark problems which tests an element's ability to model both inextensional bending and complex membrane states. Belytschko *et al.* (1985) pointed out the difficulty in passing this test. The length and radius of the full cylinder are $L=600$ and $R=300$, respectively. The thickness of the cylinder is $h=3$ and the material constants are $E=3 \times 10^7$ and $\nu=0.3$. The load applied to the cylinder at point C is $P=1$.

Due to symmetry, only one octant of the cylinder corresponding to the shaded region $ABCD$ in Fig. 18(a) is analyzed. Three triangular mesh patterns I, II, and III shown Fig. 18(b) are considered.

The solutions are obtained using $N \times N$ element meshes ($N=4, 8, 12, 16$, and 20). We consider not only meshes that are uniform but also distorted meshes, as shown in Fig. 19. When the $N \times N$ distorted mesh is used, each edge is divided by the ratio $L_1:L_2:L_3 \dots L_N = 1:2:3 \dots N$, leading to severely distorted meshes. The reference displacement at point C is $w_{ref} = -1.8248 \times 10^5$ which is given in Reference (Belytschko *et al.* 1985).

Fig. 20 presents the convergence of the normalized displacement (w_C/w_{ref}) at the position of the pinching force, point C . The best performance is obtained with the MITC3E shell element with uniform meshes and the MITC6 shell

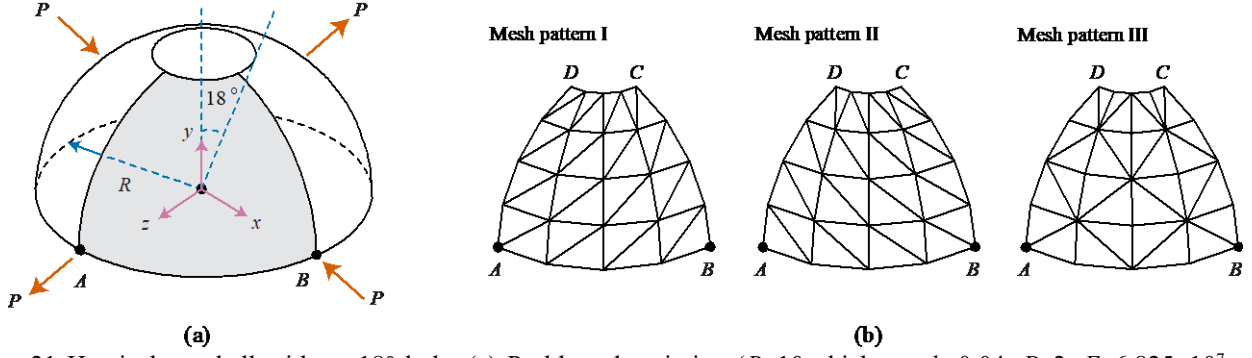


Fig. 21 Hemisphere shell with an 18° hole. (a) Problem description ($R=10$, thickness $h=0.04$, $P=2$, $E=6.825 \times 10^7$ and $\nu=0.3$). (b) Mesh patterns I, II and III used ($N=4$)

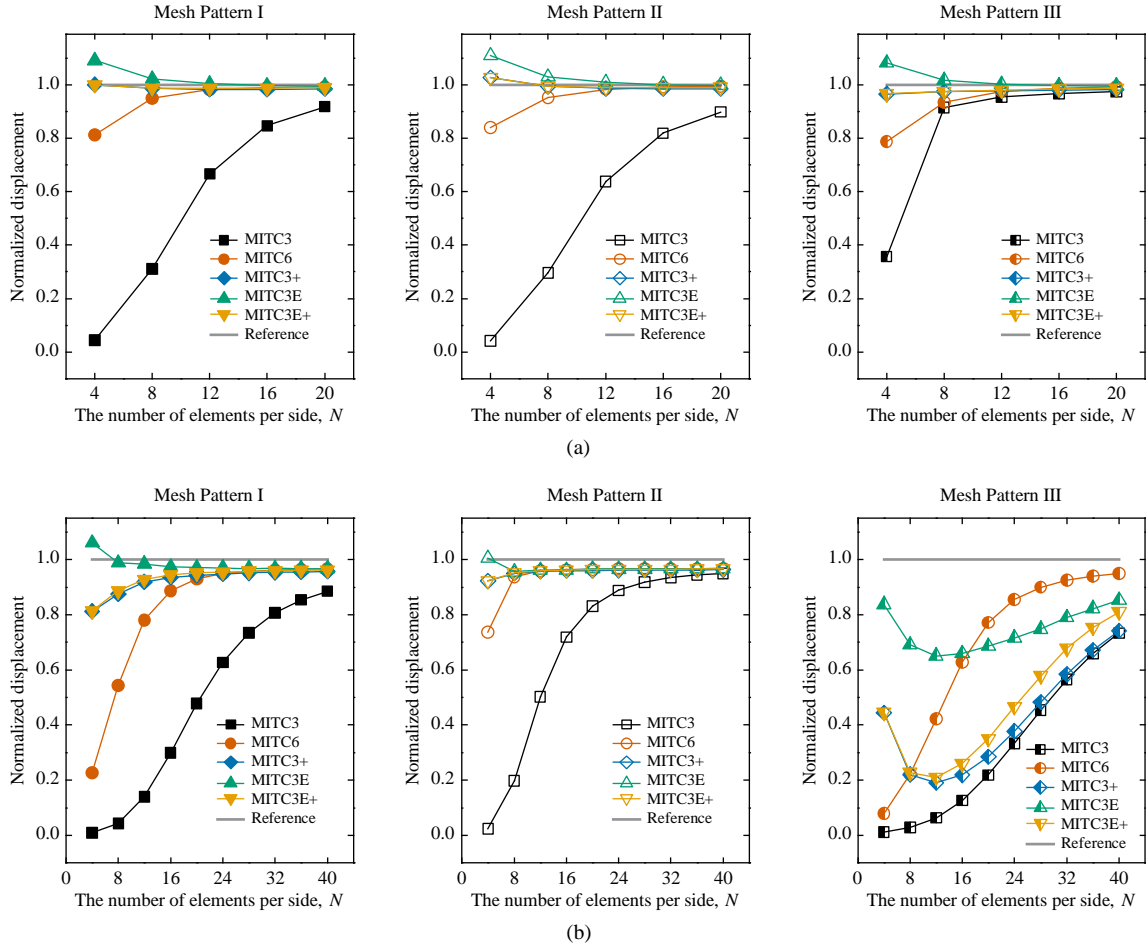


Fig. 22 Convergence of normalized displacement at point A for the hemisphere shell with the 18° hole with (a) uniform and (b) distorted meshes

element with distorted meshes, as illustrated in Fig. 20.

4.10 Hemispherical shell with an 18° hole

We consider a hemispherical shell with an 18° hole at the top shown in Fig. 21(a), which is well known as a useful problem for evaluating the ability of the element to represent rigid-body rotations and inextensible bending modes. The hemisphere has the radius $R=10$, thickness $h=0.04$, Young's modulus $E=6.825 \times 10^7$, and Poisson's ratio $\nu=0.3$. Two pairs of opposite radial concentrated loads $P=2$

are subjected along its equator. Due to symmetry, one quarter of the structure corresponding to the shaded region $ABCD$ in Fig. 21(a) is modeled and three triangular mesh patterns (I, II, and II; shown in Fig. 21(b)) are considered.

The uniform and distorted mesh patterns in Fig. 19 are considered. The solutions are obtained using $N \times N$ element meshes ($N=4, 8, 12, 16$, and 20 for uniform meshes and $N=8, 16, 24, 32$, and 40 for distorted meshes). The reference value for the radial displacement coincident at the load point (point A) is $w_{ref}=0.094$ (MacNeal and Harder 1985). The convergence of normalized displacement (w_A/w_{ref}) at

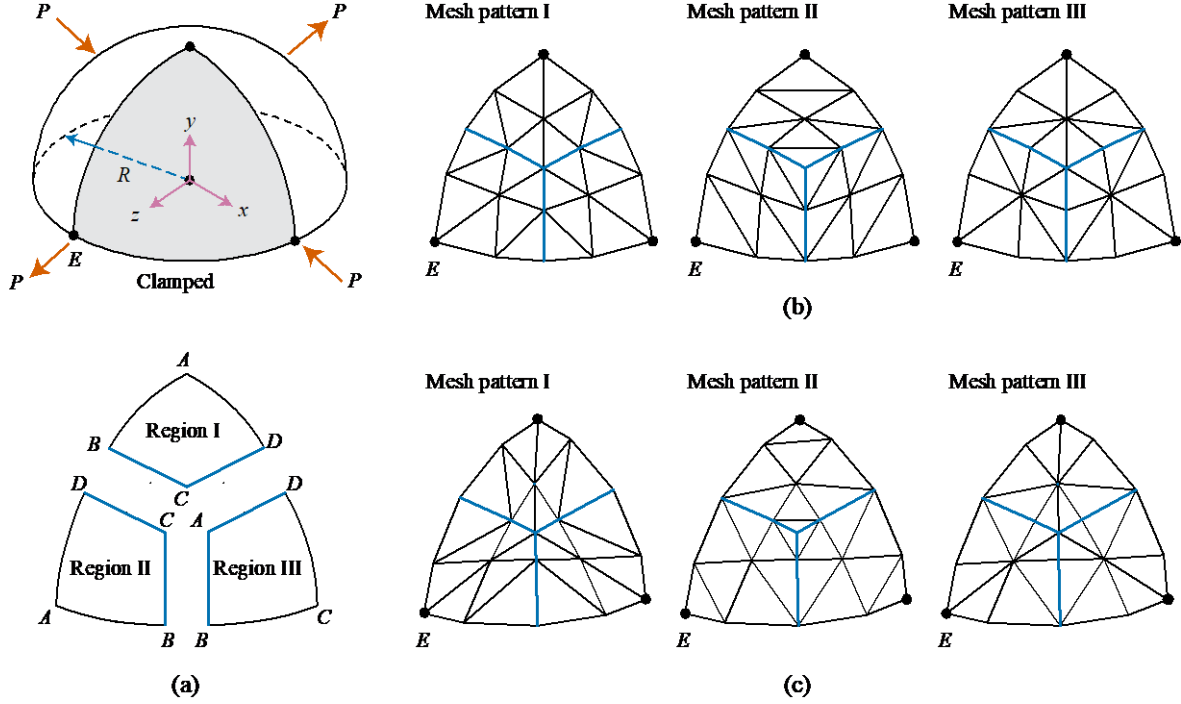


Fig. 23 Full-hemisphere shell problem. (a) Problem description ($R=10$, thickness $h=0.04$, $P=2$, $E=6.825 \times 10^7$ and $\nu=0.3$). (b) Mesh patterns I, II and III used and (c) corresponding distorted mesh patterns in Fig. 19 used here ($N=2$)

point A is presented in Fig. 22(a) for uniform meshes and in Fig. 22(b) for distorted meshes. In the study with uniform meshes, it can be observed that the results of the MITC3+ and MITC3E+ shell elements agree well with the reference solution even though the coarse mesh is used. The solution of the MITC6 shell element is significantly deteriorated due to the mesh distortion. Interestingly, with the mesh pattern III, the solution accuracy of MITC triangular shell elements significantly deteriorates even when using the finer element meshes.

4.11 Full-hemispherical problem

The shell problem considering a full hemisphere is shown in Fig. 23(a). The hemisphere has the same geometry and material properties; $R=10$, thickness $h=0.04$, Young's modulus $E=6.825 \times 10^7$, and Poisson's ratio $\nu=0.3$, which are the same properties considered in the previous problem. The hemisphere is subjected to two pairs of radial forces $P=2$. Using symmetry, one quarter of the structure corresponding to the shaded region is modeled and three triangular mesh patterns (I, II, and III; shown in Fig. 23(b)) are considered.

The solutions are obtained using the quadrant shell (shaded region) divided into three regions, $3 \times (N \times N)$ element meshes ($N=4, 8, 12, 16$, and 20). The uniform and distorted mesh patterns in Fig. 23(c) are considered. The reference displacement of $w_{ref}=0.0924$ at point E is used (Belytschko and Leviathan 1994).

The convergence of normalized displacement (w_E/w_{ref}) at point E is presented in Fig. 24(a) for uniform meshes and in Fig. 24(a) for distorted meshes. The MITC3E shell element converges well while the performance of the other

shell elements severely deteriorates when the mesh pattern III is used.

4.12 Scordelis-Lo roof

The Scordelis-Lo roof is shown in Fig. 25(a). It is a classical benchmark problem to assess the performance of shell elements. An asymptotically mixed bending-membrane behavior is observed. The roof structure is supported by rigid diaphragms at both ends. The radius of curvature is $R=25$ and the length and thickness of the roof is $L=50$ and $h=0.25$, respectively. The material has Young's modulus $E=4.32 \times 10^8$ and Poisson's ratio $\nu=0$. The roof is subjected to its self-weight. Due to symmetry, only one quarter of the shell corresponding to the shaded region $ABCD$ in Fig. 25(a) is modeled and the three mesh patterns I, II, and III shown in Fig. 25(b) are considered.

The solutions are obtained using $N \times N$ element meshes ($N=4, 8, 12, 16$, and 20). The uniform and distorted mesh patterns in Fig. 19 are used. The widely adopted reference solution for the vertical deflection at the center of the free edge (point C) is $w_{ref}=-0.3024$ (Belytschko and Leviathan 1994).

The convergence of normalized displacement (w_C/w_{ref}) at point C is presented in Fig. 26(a) for uniform meshes and in Fig. 26(b) for distorted meshes. The MITC6, MITC3E and MITC3E+ shell elements exhibit the better results even though the distorted meshes are used.

5. Conclusions

We have reviewed the formulations of the MITC

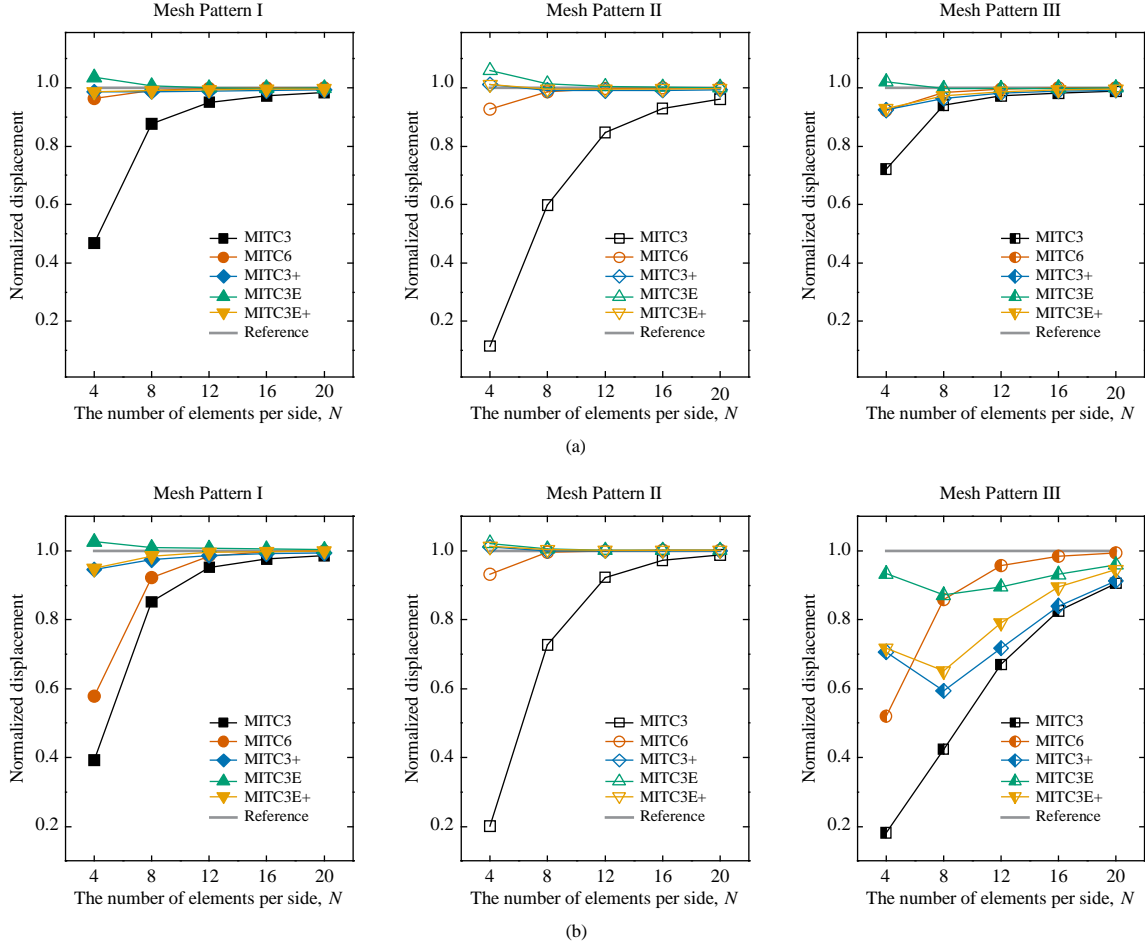


Fig. 24 Convergence of normalized displacement at point E for the full-hemisphere shell with (a) uniform and (b) distorted meshes shown in Fig. 23

triangular shell elements and compared their performance through a set of widely used benchmark problems. The benchmark tests include the plane-stress and plate problems to evaluate the ability of the partition of unity approximation and a bubble node enriching rotations. Since the solution of the triangular finite elements is highly sensitive to the triangulated patterns and distortion of the element mesh, three mesh patterns (if possible) and highly distorted meshes are used. Through the comparison of computation efficiency, as well as the convergence studies giving the displacements at some points, we can conclude as follows:

- MITC3 element: Though it is applicable to large-scale analyses requiring massive computational costs due to the numerical efficiency resulting from small non-zero entries and half-bandwidth of the stiffness matrix, the solution of the MITC3 shell element in some bending-dominated problems significantly deteriorates even when using finer uniform meshes.

- MITC6 element: The overall solutions for the MITC6 shell element are shown to be consistently better than other shell elements. However, it requires greater computational cost and additional nodes both inside and along the edge of the mesh. It is confirmed that the solutions from the MITC6 shell element are significantly deteriorated in the distorted

parameter and pre-twisted beam problems, which would be valuable to mathematically analyze the formulation to overcome the weakness.

- MITC3+ and MITC3E+ elements: The good performance of the MITC3+ shell element is verified in the bending-dominated shell problems. The significant improvement (MITC3E+ shell element) is also realized by enriching its membrane displacements. Excellent performance is observed in the bending-dominated, membrane-dominated and mixed problems.

- MITC3E element: The excellent convergence properties are validated in both membrane and bending-dominated problems even though the MITC3E shell element has a slightly large number of degrees of freedom. It is also shown that the shell element is the most robust when the distorted element meshes are used. Thus, it is promising to use the shell element locally in particular regions (such as multiple branched cracks, voids and cracks emanating from holes) with increasing few degrees of freedom. In addition, since it can increase the solution accuracy without any additional nodes or mesh refinements, it could be useful to use the shell element in place of the higher-order shell finite element.

Acknowledgments

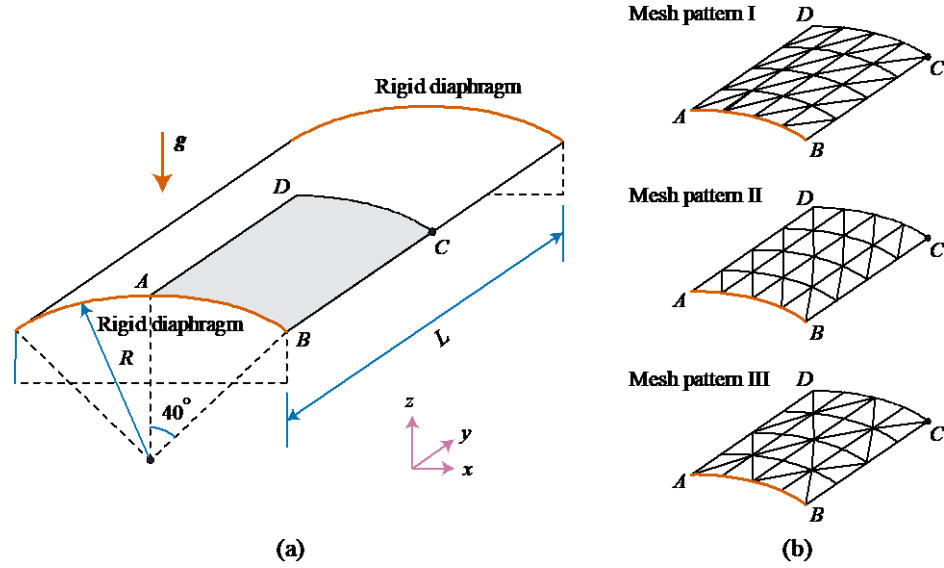


Fig. 25 Scordelis-Lo Roof problem. (a) Problem description ($L=50$, $R=25$, thickness $h=0.25$, density $\rho=360$, acceleration of gravity g with magnitude 1.0, $E=4.32 \times 10^8$ and $\nu=0$). (b) Mesh patterns I, II and III used ($N=4$)

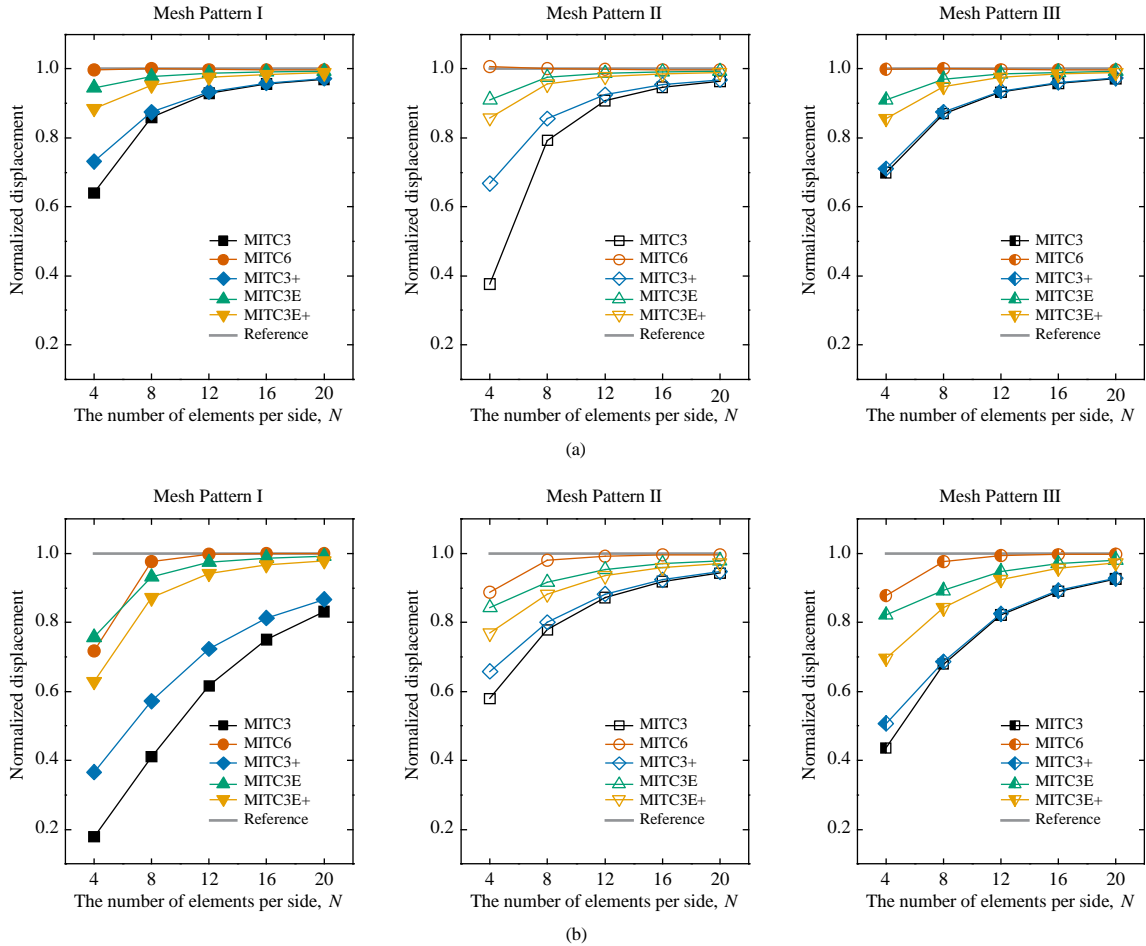


Fig. 26 Convergence of normalized displacement at point C for the Scordelis-Lo roof with (a) uniform and (b) distorted meshes shown in Fig. 19

This research was supported by a grant (KCG-01-2016-04) through the Disaster and Safety Management Institute funded by Korea Coast Guard of Korea government. This work also was supported by “Human Resources Program in

Energy Technology” of the Korea Institute of Energy Technology Evaluation and Planning (KETEP), granted financial resource from the Ministry of Trade, Industry & Energy, Republic of Korea (No. 20184030202000). Prof.

Phill-Seung Lee (Korea Advanced Institute of Science and Technology) is kindly acknowledged for his valuable comments on improving the manuscript.

References

- Andelfinger, U. and Ramm, E. (1993), "EAS-elements for two-dimensional, three-dimensional, plate and shell structures and their equivalence to HR-elements", *Int. J. Numer. Meth. Eng.*, **36**, 1311-1337.
- Babuska, I. and Melenk, J.M. (1996), "The Partition of Unity Method", *Int. J. Numer. Meth. Eng.*, **40**, 727-758.
- Bathe, K.J. (2016), *Finite Element Procedures*, 2nd Edition, 2014 and Higher Education Press, China.
- Bathe, K.J. and Dvorkin, E.N. (1986), "A formulation of general shell elements the use of mixed interpolation of tensorial components", *Int. J. Numer. Meth. Eng.*, **22**, 697-722.
- Bathe, K.J., Lee, P.S. and Hiller, J.F. (2003), "Towards improving the MITC9 shell element", *Comput. Struct.*, **81**, 477-489.
- Belytschko, T. and Leviathan, I. (1994), "Physical stabilization of the 4-node shell element with one point quadrature", *Comput. Meth. Appl. Mech. Eng.*, **113**, 321-350.
- Belytschko, T., Stolarski, H., Liu, W.K., Carpenter, N. and Ong, J.S.J. (1985), "Assumed strain stabilization procedure for the 9-node Lagrange shell element", *Comput. Meth. Appl. Mech. Eng.*, **51**, 221-258.
- Belytschko, T., Wong, B.L. and Stolarski, H. (1989), "Assumed strain stabilization procedure for the 9-node Lagrange shell element", *Int. J. Numer. Meth. Eng.*, **28**, 385-414.
- Chapelle, D. and Suarez, I.P. (2008), "Detailed reliability assessment of triangular MITC elements for thin shells", *Comput. Struct.*, **86**, 2192-2202.
- Choi, C.K. and Paik, J.G. (1994), "An efficient four node degenerated shell element based on the assumed covariant strain", *Struct. Eng. Mech.*, **2**(1), 17-34.
- Choi, C.K., Lee, P.S. and Park, Y.M. (1999), "Defect-free 4-node flat shell element: NMS-4F element", *Struct. Eng. Mech.*, **8**(2), 207-231.
- Cook, R.D. (2007), *Concepts and Applications of Finite Element Analysis*, John Wiley & Sons.
- Da Veiga, L.B., Chapelle, D. and Suarez, I.P. (2007), "Towards improving the MITC6 triangular shell element", *Comput. Struct.*, **85**, 1589-1610.
- Duarte, C.A. and Oden, J.T. (1996), "An hp adaptive method using clouds", *Comput. Meth. Appl. Mech. Eng.*, **139**, 237-262.
- Duarte, C.A., Babuska, I. and Oden, J.T. (2000), "Generalized finite element methods for three dimensional structural mechanics problems", *Comput. Struct.*, **77**, 215-232.
- Duarte, C.A., Hamzeh, O.N., Liszka, T.J. and Tworzydło, W.W. (2001), "The design and analysis of the generalized finite element method", *Comput. Meth. Appl. Mech. Eng.*, **190**, 2227-2262.
- Han, S.C., Kanok-Nukulchai, W. and Lee, W.H. (2011), "A refined finite element for first-order plate and shell analysis", *Struct. Eng. Mech.*, **20**(2), 191-213.
- Hughes, T.J.R. (2012), *The Finite Element Method: Linear Static and Dynamic Finite Element Analysis*, Courier Corporation.
- Jeon, H.M., Lee, P.S. and Bathe, K.J. (2014), "The MITC3 shell finite element enriched by interpolation covers", *Comput. Struct.*, **134**, 128-142.
- Jeon, H.M., Lee, Y., Lee, P.S. and Bathe, K.J. (2015), "The MITC3+ shell element in geometric nonlinear analysis", *Comput. Struct.*, **146**, 91-104.
- Jun, H., Yoon, K., Lee, P.S. and Bathe, K.J. (2018), "The MITC3+ shell element enriched in membrane displacements by interpolation covers", *Comput. Meth. Appl. Mech. Eng.*, **337**, 458-480.
- Karypis, G. and Kumar, V. (1998), "A fast and high quality multilevel scheme for partitioning irregular graphs", *SIAM J. Sci. Comput.*, **20**, 359-392.
- Kim, D.N. and Bathe, K.J. (2009), "A triangular six-node shell element", *Comput. Struct.*, **87**, 1451-1460.
- Kim, J. and Bathe, K.J. (2013), "The finite element method enriched by interpolation covers", *Comput. Struct.*, **116**, 35-49.
- Kim, S. and Lee, P.S. (2018), "A new enriched 4-node 2D solid finite element free from the linear dependence problem", *Comput. Struct.*, **202**, 25-43.
- Ko, Y., Lee, P.S. and Bathe, K.J. (2016), "The MITC4+ shell element and its performance", *Comput. Struct.*, **169**, 57-68.
- Ko, Y., Lee, P.S. and Bathe, K.J. (2017), "A new MITC4+ shell element", *Comput. Struct.*, **182**, 404-418.
- Ko, Y., Lee, Y., Lee, P.S. and Bathe, K.J. (2017), "Performance of the MITC3+ and MITC4+ shell elements in widely-used benchmark problems", *Comput. Struct.*, **193**, 187-206.
- Lee, P.S. and Bathe, K.J. (2004), "Development of MITC isotropic triangular shell finite elements", *Comput. Struct.*, **82**, 945-962.
- Lee, P.S., Noh, H.C. and Choi, C.K. (2008), "Geometry-dependent MITC method for a 2-node iso-beam element", *Struct. Eng. Mech.*, **29**, 203-221.
- Lee, Y., Jeon, H.M., Lee, P.S. and Bathe, K.J. (2015), "The modal behavior of the MITC3+ triangular shell element", *Comput. Struct.*, **153**, 148-164.
- Lee, Y., Lee, P.S. and Bathe, K.J. (2014), "The MITC3+ shell element and its performance", *Comput. Struct.*, **138**, 12-23.
- Lee, Y., Yoon, K. and Lee, P.S. (2012), "Improving the MITC3 shell finite element by using the Hellinger-Reissner principle", *Comput. Struct.*, **110**, 93-106.
- MacNeal, R.H. and Harder, R.L. (1985), "A proposed standard set of problems to test finite element accuracy", *Fin. Elem. Anal. Des.*, **1**, 3-20.
- Melenk, J.M. and Babuska, I. (1996), "The partition of unity finite element method: Basic theory and applications", *Comput. Meth. Appl. Mech. Eng.*, **139**, 289-314.
- Morley, L.S.D. (1963), *Skew Plates and Structures*, Pergamon Press, New York, U.S.A.
- Oden, J.T., Duarte, C.A. and Zienkiewicz, O.C. (1998), "A new cloud-based hp finite element method", *Comput. Meth. Appl. Mech. Eng.*, **153**, 117-126.
- Schenk, O. and Gartner, K. (2006), "On fast factorization pivoting methods for sparse symmetric indefinite systems", *Electr. Trans. Numer. Anal.*, **23**, 158-179.
- Strouboulis, T., Babuska, I. and Copps, K. (2000), "The design and analysis of the generalized finite element method", *Comput. Meth. Appl. Mech. Eng.*, **181**, 43-69.
- Strouboulis, T., Copps, K. and Babuska, I. (2000), "The generalized finite element method: An example of its implementation and illustration of its performance", *Int. J. Numer. Meth. Eng.*, **47**, 1401-1417.
- Tian, R., Yagawa, G. and Terasaka, H. (2006), "Linear dependence problems of partition of unity-based generalized FEMs", *Comput. Meth. Appl. Mech. Eng.*, **195**, 4768-4782.
- Timoshenko, S.P. and Goodier, J.N. (1970), *Theory of Elasticity*, McGraw-Hill, New York, London.
- Timoshenko, S.P. and Woinowsky-Krieger, S. (1959), *Theory of*

Plates and Shells, McGraw-hill.

- Xu, J.P. and Rajendran, S. (2013), "A 'FE-Meshfree' TRIA3 element based on partition of unity for linear and geometry nonlinear analyses", *Comput. Mech.*, **51**, 843-864.
- Yoo, S.W. and Choi, C.K. (2000), "Geometrically nonlinear analysis of laminated composites by an improved degenerated shell element", *Struct. Eng. Mech.*, **9**(1), 99-110.

PL